Title: Kinesin-1 Autoinhibition Tunes Cargo Transport by Motor Ensembles

Authors: Brandon M. Bensel[1], Samantha B. Previs[1], Patricia M. Fagnant[1], Kathleen M. Trybus[1], Sam Walcott*[,2], and David M. Warshaw*[,1]

Author Affilitations:

1. Department of Molecular Physiology and Biophysics, University of Vermont Larner College of Medicine, Burlington, VT 05405
2. Department of Mathematical Sciences, and Bioinformatics and Computational Biology, Worcester Polytechnic Institute, Worcester, MA 01609

*Co-corresponding Authors:

David M. Warshaw
University of Vermont
Dept. of Mol. Physiology & Biophysics
Health Science Research Facility
Burlington, VT 05405
(802)-656-4300
David.warshaw@med.uvm.edu

Sam Walcott
Worcester Polytechnic Institute
Dept. of Mathematical Sciences
Bioinformatics and Computational Biology
Worcester, MA 01609
swalcott@wpi.edu

**Abstract**

Intracellular vesicular transport by kinesin-1 motors through numerous 3-dimensional (3D) microtubule (MT) intersections must be regulated to support proper vesicle delivery. Knowing kinesin-1 can be regulated via autoinhibition, does kinesin-1 exhibit autoinhibition on cargo, and could this regulate vesicular transport through 3D MT intersections *in vitro*? To answer this question, we compared liposome transport by ~10 nearly full-length kinesin-1 motors with KLC bound (Kin∆C) versus constitutively active control (K543). In 3D MT intersections, Kin∆C-liposomes terminate (48%), go straight (43%), but rarely turn (9%), starkly contrasting K543-liposomes which go straight (57%), turn (31%), but rarely terminate (12%). On single MTs, Kin∆C-liposomes have reduced run lengths and detachment forces versus K543-liposomes, suggesting autoinhibition reduces MT engagement, as supported by 3-fold lower Kin∆C MT landing rates versus K543, and mechanistic *in silico* modeling. Furthermore, kinesore, a small molecule that overcomes kinesin-1 autoinhibition, restores Kin∆C's MT engagement. Thus, we propose that partial kinesin-1 autoinhibition while cargo-bound may fine-tune cargo delivery to support physiological demands.

**Summary**

Vesicular transport by kinesin-1 motors through the cell's 3-dimensional (3D) microtubule (MT) network is regulated to ensure proper cargo delivery. Dynamic autoinhibition of kinesin-1 motors, which are bound to cargo, fine-tunes liposome transport through 3D MT intersections *in vitro*.

## Introduction

Secreted and transmembrane proteins are sorted within the Golgi network into vesicles that are transported by kinesin-1 (KIF5) motors along microtubules (MTs) to their destination on the plasma membrane (Coy et al., 1999; Vale, 2003; Heaslip et al., 2014; Cai et al., 2007; Hirokawa et al., 2009; Hirokawa and Tanaka, 2015; Fourriere et al., 2020). To meet the cell's physiological demands, vesicular transport and delivery must be regulated spatially and temporally (Heaslip et al., 2014; Barlan and Gelfand, 2017). Although multiple mechanisms exist to regulate how kinesin-1 motor teams maneuver vesicular cargo through the complex 3-dimensional (3D) MT network (Friedman and Vale, 1999; Reilein et al., 2001; Verhey and Hammond, 2009), the most basic mode of regulation is by activating or inhibiting individual motors (Ross et al., 2008; Verhey and Hammond, 2009). Heterotetrameric kinesin-1, consisting of two heavy chains (KHC) and two kinesin light chains (KLC) (Vale et al., 1985; Verhey et al., 2011), adopts a "folded", autoinhibited state with numerous intramolecular interactions along the length of the KHC (Coy et al., 1999; Weijman et al., 2022; Chiba et al., 2022; Tan et al., 2023; Carrington et al., 2024). The KLCs further stabilize the inhibited state by forming a 6-helix bundle with the KHC near the hinge 2 region (Cai et al., 2007; Weijman et al., 2022; Chiba et al., 2022; Tan et al., 2023). Cargo binding to KHC's C-terminal domains or KLC is thought to disrupt these autoinhibitory interactions, allowing the motor to become "extended" and active (i.e., able to engage the MT) (Chiba et al., 2022). However, once bound to cargo, is kinesin-1 stably active, or is it in an equilibrium between the autoinhibited "folded" and active "extended" states, which could be tuned to optimize cargo transport and delivery by kinesin-1 motor teams (Fu and Holzbaur, 2014; Barlan and Gelfand, 2017)?

Here we reconstitute vesicular cargo transport *in vitro* to determine if kinesin-1 autoinhibition affects multimotor transport of physiologically relevant, 350-nm diameter, fluid-like liposomes through suspended 3D MT intersections (Bensel et al., 2024), much like those encountered in cells (Bálint et al., 2013; Lakadamyali, 2014; Osunbayo et al., 2015; Verdeny-

Vilanova et al., 2017). We took advantage of our previously characterized, nearly full-length (1-888 amino acids) kinesin-1 construct (Kin∆C) with bound KLC that lacks the so-called IAK region near the C-terminus that is necessary for full inhibition of activity, but retains the hinge region in the coiled coil that allows the molecule to bend and engage in a head–tail interaction (Lu et al., 2009). Directional outcomes in 3D MT intersections for liposomes transported by teams of ~10 Kin∆C motors were in stark contrast to those of liposomes transported by teams of a constitutively active truncated kinesin-1 lacking KLC (K543) (Bensel et al., 2024). Specifically, Kin∆C-liposomes either went straight through or terminated in intersections, but rarely turned onto the intersecting MT. K543-liposomes, preferred to go straight rather than turn, but rarely terminated in the intersection (Bensel et al., 2024). These differences in directional outcomes may be due to the autoinhibition of the cargo-bound Kin∆C motors effectively reducing the number of motors available to engage the MT (Lu et al., 2009; Chiba et al., 2022; Tan et al., 2023). This hypothesis is supported by the observation that cargos transported by Kin∆C ensembles along single MTs have shorter run lengths and generate less force against an optical trap compared to K543 ensembles. Treating Kin∆C with kinesore, a small molecule that binds KLC and activates kinesin-1 (Randall et al., 2017), causes the motor to adopt a more “extended” conformation, making Kin∆C MT engagement and transport identical to constitutively active K543 motors. To explain why Kin∆C autoinhibition modulates liposome transport in 3D MT intersections, we modified our previously published *in silico* mechanistic model of kinesin-1 transport (Bensel et al., 2024) to implicitly include autoinhibition. The model reproduces our observations of liposome transport through 3D MT intersections by Kin∆C when modified either by reducing the number of active motors in the ensemble or reducing the maximum rate of MT association, supporting our hypothesis. We propose that kinesin-1 autoinhibition provides the cell with a mechanism to expand and fine tune its dynamic range of potential cargo transport and delivery properties.

## Results and Discussion

### *KinΔC-liposomes go straight or terminate but rarely turn in 3D MT intersections.*

Kinesin-1 motors must navigate their vesicular cargo through multiple 3D MT intersections en route to the cargo's destination (Bálint et al., 2013; Lakadamyali, 2014; Osunbayo et al., 2015; Verdeny-Vilanova et al., 2017). If kinesin-1 motors exist in an equilibrium between the autoinhibited and active states (Fig. 1A) while attached to a vesicle, does this equilibrium impact how the vesicle is maneuvered through a MT intersection? To address this question *in vitro,* we suspended MTs between poly-L-lysine-coated silica beads on a coverslip surface, creating orthogonal 3D MT intersections (Fig. 1B and C). We then decorated 350-nm fluid-like (DOPC) liposomes (Fig. 1B) with one of two kinesin-1 constructs that could freely diffuse on the liposome surface, which were present at ~10 motors per liposome, based on a photobleaching-based counting assay (Fig. S1). The ubiquitously expressed murine kinesin-1 heavy chain, KIF5B, was the basis for both constructs (Fig. 1A). The KinΔC construct (1-888 amino acids) with full-length KLC2 bound, retains the capacity to be partially autoinhibited, based on a 3-fold lower landing rate compared with the constitutively active truncated construct K543 (Fig. 3C). Both constructs are C-terminally biotinylated to provide an attachment handle to the liposome (Lu et al., 2009; Bensel et al., 2024).

Using 3D stochastic optical reconstruction microscopy (STORM), the liposome's spatial relationship to the MT intersection was defined, i.e., the liposome approach angle (α) and vertical gap (*d*) between the MTs (Fig. 1B and C) (Lombardo et al., 2017; Bensel et al., 2024). This ensured that we only considered directional outcomes (i.e., whether the liposome went straight (Fig. 1D, Video S1), turned (Fig. 1E, Video S2), or terminated its run) that resulted from motors on the liposome surface being able to reach the intersecting MT. For each event that met our criteria, we recorded if the liposome paused, how long it paused, and the directional outcome.

At 3D MT intersections, Kin∆C-liposomes were nearly as likely to terminate (48%) as to go straight (43%) but rarely turned onto the crossing MT (9%) (Fig. 1F). These directional outcomes were distinctly different than we previously reported for K543-liposomes, which preferred to go straight (58%) or turned occasionally onto the crossing MT (37%), but rarely terminated (5%) (Fig. 1F) (Bensel et al., 2024). Could pausing in the intersection offer insight to these constructs' different directional outcomes? In fact, Kin∆C-liposomes were less likely to pause (48% paused) compared to K543-liposomes (70% paused) (Bensel et al., 2024), but when paused their lifetimes (6.1 sec) were 36% longer (Fig. 1G). Our previous *in silico* modeling of K543 transport in 3D MT intersections suggested that pausing originates from motors on the liposome surface binding simultaneously to both MTs and engaging in a tug-of-war, which must be resolved before a directional outcome is determined (Osunbayo et al., 2015; Bergman et al., 2018; Bensel et al., 2024). The observation that Kin∆C-liposomes rarely turn suggests that the motors' autoinhibition reduces the number of available Kin∆C motors that can engage the crossing MT resulting in less frequent tug-of-wars, pausing, and turning events. If resolving a tug-of-war requires MT engagement of a new motor, a reduction in the number of available motors would also prolong these events resulting in longer pauses.

***Kin∆C ensembles have reduced MT engagement.***

For kinesin-1 transported cargoes, the run length, or characteristic travel distance, scales with the number of motors that are MT-engaged (Gross et al., 2007; Vershinin et al., 2007; Furuta et al., 2013; Feng et al., 2018), while velocity slows due to mechanical coupling creating internal loads between the motors (Rogers et al., 2009; Jamison et al., 2010; Bensel et al., 2024). Therefore, we measured Kin∆C-liposome run lengths and velocities along single MTs adhered to a glass slide for varying size Kin∆C ensembles (~5, ~10, or ~20 motors, Fig. 2A) compared to a single Kin∆C motor transporting a quantum dot (Qdot) cargo. As expected, Kin∆C ensembles universally had longer run lengths (1.99 – 2.98 μm) and slower velocities (637

– 702 nm/s) than single Kin∆C motors (1.19 μm and 890 nm/s) (Fig. 2B and C). However, compared to K543-liposomes transported by similar ensemble sizes, Kin∆C-liposomes had shorter median run lengths (Fig. 2B, Table S1), although velocities were similar (Fig. 2C, Table S1). In fact, these run length differences may be underestimated, as run lengths can be limited by the MT length itself (Mayr et al., 2011; McKenney et al., 2014; Soppina et al., 2014). Knowing that MTs were prepared identically with similar length distributions (Fig. S2), we compared the frequency at which liposomes reached the MT end (Fig. 2D). For all motor ensemble sizes, K543-liposomes were ~46% more likely than Kin∆C-liposomes to reach the MT end (Fig. 2D), suggesting that the K543-liposomes run lengths are more highly underestimated than those of the Kin∆C-liposomes. Therefore, the reduction in Kin∆C-liposome run lengths compared to K543-liposomes is even greater. These data support the hypothesis that fewer Kin∆C motors from the ensemble engage the MT compared to the constitutively active K543 control.

To effectively count how many Kin∆C motors in the ensemble are MT engaged, we measured the cargo's detachment force in an optical trapping assay, as this force should scale with the engaged motor number (Vershinin et al., 2007; Hendricks et al., 2012; Furuta et al., 2013) (Fig. 2E). Therefore, we incubated 500-nm lipid-coated beads with 20-fold excess Kin∆C to match the motor density of a 350-nm liposome with 10 bound motors and then measured the detachment force as the Kin∆C motors step against the hindering load of the trap (Fig. 2E and F). The Kin∆C-bead detachment forces were distributed as the sum of two Gaussians centered at 6.5 and 12.6 pN, with 80% of the events in the first peak (Fig. 2G), whereas K543-bead detachment forces were described by a triple Gaussian with peaks at 5.7, 11.4, and 16.4 pN (Fig. 2H). The initial detachment force peaks for the Kin∆C and K543 constructs were equivalent to that measured for a single motor (Kin∆C: 6.4 ± 1.9 pN; K543: 5.7 ± 1.1 pN) (Fig. 3E and F) and similar to that in the literature (Visscher et al., 1999; Schnitzer et al., 2000; Schroeder et al., 2012). Therefore, often only 1 but at most 2 Kin∆C motors are MT engaged compared to K543

ensembles where up to 3 motors can be MT engaged. These data once again suggest that autoinhibition effectively reduces the number of active motors.

***KinΔC has a reduced MT landing rate but once MT engaged is indistinguishable from K543.***

If kinesin-1 can transition between autoinhibited and active states, does this dynamic equilibrium affect how often the motor engages a MT and its motile properties once engaged with the MT? To quantify MT engagement, we measured the landing rate (number of processive runs per unit time per unit MT length) of single Qdot-labelled KinΔC (1 nM) relative to K543 (1 nM) in saturating MgATP (Fig. 3A and C). KinΔC initiated processive runs at a rate (0.08 $\mu m^{-1}$ $min^{-1}$) ~3-fold less than K543 (0.23 $\mu m^{-1}$ $min^{-1}$) (Fig. 3B and C, Video S3), suggesting that kinesin-1 autoinhibition reduces MT engagement. Once engaged, the mechanochemical properties of single KinΔC motors were not impacted by autoinhibition, with median run lengths (RL), mean velocities (V) and detachment forces (F) (Fig. 3D) (RL= 1.19 μm; V=890 nm/s; F= 6.4 ± 1.9 pN) (Fig. 2B and C, Fig. 3E) that were indistinguishable from K543 (RL= 1.19 μm; V= 868 nm/s; F= 5.7 ± 1.1 pN) (Fig. 2B and C, Fig. 3F). Once KinΔC engages with the MT, the motor's processivity and force generation are governed by the mechanochemistry of the fully active motor, suggesting that transitions back into the autoinhibited state must occur only in solution, following MT detachment. If the reduced rate of MT association reflects a dynamic equilibrium between the autoinhibited and active states, these data do not inform how rapidly the two states exchange (see modeling section below). Nonetheless, the reduced landing rate of KinΔC suggests that autoinhibition can effectively reduce the number of MT engaged motors in an ensemble and thus the ensemble's cargo transport capacity as described above.

***Kinesore treatment activates an autoinhibited KinΔC motor.***

If autoinhibitory intramolecular interactions are responsible for KinΔC's reduced MT engagement, disrupting these interactions should activate the motor. To test this idea we used

kinesore, a small molecule that interacts with the KLC to mimic cargo binding and disrupt inhibitory intramolecular interactions to activate kinesin-1 (Randall et al., 2017; Angerani et al., 2021). In the presence of 50 μM kinesore, KinΔC's landing rate increased significantly to 0.26 $\mu m^{-1}$ $min^{-1}$, equal to that of K543 (0.22 $\mu m^{-1}$ $min^{-1}$) (Fig. 4A and B, Video S3 and S4), which was unaffected by kinesore as this construct lacks KLC. By restoring the KinΔC MT landing rate, would kinesore treatment of a KinΔC ensemble increase its force-bearing capacity (i.e., increased number of MT-engaged motors)? This was in fact the case as the distribution of detachment forces measured for KinΔC-beads in the optical trap with 50 μM kinesore present was now best fit by the sum of three rather than two Gaussians, centered at 7.2 pN, 13.7 pN, and 20.0 pN (Fig. 4C and D), similar to that for K543-beads (Fig. 2H). Therefore, the number of MT engaged KinΔC motors increased from at most 2 in the absence of kinesore to up to 3 engaged motors with kinesore present.

Implicit in the activation of KinΔC by kinesore is that disrupting the autoinhibitory intramolecular interactions should result in a more extended molecule (Randall et al., 2017; Weijman et al., 2022; Tan et al., 2023). We utilized size exclusion chromatography to assess the relative shape of KinΔC molecules in the presence or absence of 50 μM kinesore. A molecule with an extended structure elutes sooner than a molecule of the same molecular mass with a folded structure (Fig. 4E). Elution fractions from the size exclusion chromatography column equilibrated and eluted in the absence (Fig. 4E, top) versus presence of 50 μM kinesore (Fig. 4E, bottom) show that KinΔC elutes earlier in the presence of kinesore. These data suggest that kinesore binding to KLC results in a more extended conformation, consistent with an active KinΔC motor.

***KinΔC autoinhibition: mechanistic model and impact on liposome transport.***

The transport data for single KinΔC motors and ensembles together suggest that KinΔC can adopt the folded and extended states even when attached to cargo. To understand how

Kin∆C autoinhibition impacts ensemble transport, we took advantage of our previously published mechanistic *in silico* model that predicted single motor and ensemble K543 transport (Fig. 5A) on single MTs and in 3D MT intersections (see Methods for details of simulations) (Bensel et al., 2024). Crucially, the model is predictive because it is constrained only by a three-state model of kinesin's mechanochemistry (Andreasson et al., 2015) and the physical properties of the liposomes and MTs. Adopting this model to predict Kin∆C transport was simplified knowing that once engaged with the MT, the mechanochemical properties of Kin∆C are identical to K543. Therefore, the *in silico* model was modified to include Kin∆C autoinhibition as a dynamic equilibrium between an inhibited and an active state where the exchange rates between states are either slow on the timescale of the simulation such that Kin∆C exists predominantly in the inhibited state (i.e. effectively reducing the number of active motors in the ensemble) (Fig. 5E) or the exchange rates are much faster than the timescale of the simulation such that autoinhibition can be modeled simply as a reduced apparent attachment rate (Fig. 5F). In support of these two concepts, others in the field have proposed both motor number (D'Souza et al., 2023) and reattachment kinetics (Feng et al., 2018; Gicking et al., 2022) as important determinants of ensemble transport properties.

For single Kin∆C motors, the model predicts run lengths, velocity, and detachment forces (RL= 1.66 μm; V= 787 nm/s; F= 6.5 pN) as observed experimentally and as reported previously for K543 (Bensel et al., 2024) (Fig. 5B-D). To model autoinhibition and its effect on Kin∆C MT engagement, we assumed that the 3-fold lower Kin∆C MT landing rate compared to K543 (Fig. 3C) was due to autoinhibition, as supported by the observation that kinesore restores the landing rate of Kin∆C to that of K543 (Fig. 4B). Therefore, we first ran liposome transport simulations, as described above, with autoinhibition reducing the number of active motors in the ensemble by a factor of 3 to model a slow exchange rate between the active and inhibited states (Fig. 5E). Since liposomes were decorated with a 10-motor ensemble, we simulated

liposome transport by either 3 or 4 motors and combined the results for each transport condition to best reflect the desired 3.33 motors (i.e. 10 motors divided by a factor of 3). Alternatively, we set the maximum MT attachment rate ($k_{a,0} = 50\text{s}^{-1}$) for all motors in the ensemble to 1/3 of the rate which predicted the K543 observations ($k_{a,0} = 150\text{s}^{-1}$), reflecting a 3-fold reduction in the apparent attachment rate and modeling rapid exchange between the active and inhibited states (Fig. 5F).

Simulations for reduced motor number and MT attachment rate reproduced the experimental trends in ensemble run lengths and velocities for Kin∆C versus K543 (Fig. 5G and H). Interestingly, the reduced motor number simulations were consistent with the experimentally observed detachment force distributions showing most often 1 or at most 2 MT engaged Kin∆C motors (Fig. 5I). Simulations with a reduced MT attachment rate, although broadly similar to the reduced motor number case, did have a minor population of 3 simultaneously engaged motors, though less frequently than in the active model (Fig. 5I). For Kin∆C-liposomes in 3D MT intersections, both the reduced motor number and MT attachment rate simulations qualitatively reproduced the predominant directional outcomes of going straight through or terminating in the intersection that were dramatically different than the K543-liposome directional outcomes and those predicted by a model of fully active motors (Fig. 5J) (Bensel et al., 2024).

To understand why reduced motor number or MT association rate affects directional outcomes in 3D MT intersections, we must rely on our *in silico* model to provide a mechanistic basis for how each directional outcome occurs. In brief, as a liposome enters the intersection, motors on the liposome surface can bind simultaneously to both MTs and thus the liposome may pause if the motors engage in a tug-of-war. In a tug-of-war, motors stochastically attach and detach from both MTs with the tug-of-war resolved when motors on one of the intersecting MTs all detach, allowing the winning team to pull the liposome straight (Video S5) or turn (Video S7). Generally, if no tug-of-war occurs, the liposome proceeds straight (Video S6). Finally, if all

MT engaged motors detach, transport is terminated (Video S8). If we reduce motor-MT engagement by either reducing the number of available motors or the MT attachment rate, a tug-of-war is less likely to occur, favoring straight outcomes. Furthermore, since both experimental and simulated data suggest that Kin∆C-liposome transport is driven most often by a single engaged motor, when the liposome collides with the crossing MT the motor may detach, terminating the run (Video S9). Thus, our model provides a mechanistic basis for kinesin autoinhibition impacting directional outcomes at 3D MT intersections. Interestingly, modelling autoinhibition as an equilibrium between a folded and extended state where the exchange rates between the states are either slow or rapid (see above) captures much of the Kin∆C transport behavior (Fig. 5), suggesting that this mode of motor regulation is not sensitive to the exchange rates. However, the detachment force distribution is better predicted by the model of slow exchange rates suggesting that the folded, autoinhibited state resulting from multiple intramolecular interactions is most likely quite stable, as reported in the literature (Chiba et al., 2022; Weijman et al., 2022; Tan et al., 2023; Carrington et al., 2024).

**Conclusion**

Here we provide evidence that kinesin-1 autoinhibition has profound effects on liposome transport *in vitro* whether it be on a single MT or when challenged by a 3D MT intersection. The partial autoinhibition exhibited by the Kin∆C construct is only one example of what is likely a range of motor activation that is possible in cells and depends on kinesin-1 isoform (Chiba et al., 2022), whether or not KLCs are bound (Chiba et al., 2022; Tan et al., 2023), the cargo adapter that kinesin is bound to (Fu and Holzbaur, 2014; Chiba et al., 2022), as well as MAPs such as MAP7 that enhance engagement of kinesin with the MT (Monroy et al., 2020; Ferro et al., 2022; Chiba et al., 2022). While this study focuses on kinesin-1, the mechanochemical differences in kinesin subfamilies may provide the cell additional capacity to tune cargo transport (Soppina and Verhey, 2014; Gilbert et al., 2018; Gicking et al., 2022). Given the cell's

3D MT network with numerous intersections, optimizing the directional outcome at each intersection, which is sensitive to the effective number of active motors, provides the cell a mechanism for ensuring vesicular cargo delivery to the proper destination.

## Materials and Methods

*Kinesin motor constructs and purification.*

Two kinesin motor constructs were used in this study, Kin∆C and K543. Kin∆C contains the N-terminal 888 amino acids of the mouse KIF5B kinesin heavy chain (accession number: Q61768), co-expressed with full-length mouse kinesin light chain KLC2 (accession number: BC014845). K543 contains the N-terminal 543 amino acids of the mouse KIF5B kinesin heavy chain (accession number: Q61768) followed by a biotin ligase recognition sequence and FLAG tag used for purification. The biotin ligase recognition sequence used in both constructs is an 88 amino acid sequence from the E. coli biotin carboxyl carrier protein, and is singly biotinylated during expression (Cronan, 1990).

Both kinesin constructs were expressed and purified from the baculovirus/Sf9 cell system. To express Kin∆C, Sf9 cells were infected with two recombinant baculoviruses, one encoding the sequence of the Kin∆C heavy chain, the other encoding full-length KLC2. Each baculovirus was used at a ratio of 5 viral particles per cell. The infected cells were grown and lysed in media supplemented with 0.2 mg/ml biotin for 72 hours prior to harvesting and lysis by sonication in lysis buffer (10 mM imidazole, pH 7.4, 0.3 M NaCl, 1 mM EGTA, 5 mM $MgCl_2$, 7% (w/v) sucrose, 2 mM DTT, 0.5 mM 4-(2-aminoethyl)benzenesulfonyl fluoride, 5 µg/ml leupeptin). The cell lysate was clarified by ultracentrifugation at 200,000 x g for 40 minutes, and the K543 protein was purified from the resultant supernatant by FLAG affinity chromatography. Importantly, prior work demonstrated that this strategy yields a 1:1 stoichiometry of KLC to Kin∆C heavy chain in the final sample (Lu et al., 2009; Ali et al., 2008). To express K543, Sf9

cells were infected with a recombinant baculovirus encoding the sequence of K543, the biotin ligase recognition sequence, and the FLAG tag, at a ratio of at least 5 viral particles per Sf9 cell. The infected cells were grown and lysed as described above and expressed protein as purified from the cell lysate as described above. Additional kinesin constructs with an encoded YFP were expressed and purified as described above for motor counting experiments. For motor counting Kin∆C, a C-terminal YFP was added to the KLC2, while K543 was made with an N-terminal YFP. Kinesin aliquots were in 10mM Imidazole (pH = 7.4) with 200 mM NaCl, 55% glycerol, 1 mM DTT, 1μg/ml Leupeptin, and 50 μM MgATP. Aliquots were flash frozen prior to storage at -80° C.

*Microtubule preparation.*

Microtubules (MTs) were prepared using a mixture of unlabeled porcine brain tubulin (Cytoskeleton) with rhodamine labelled tubulin (Cytoskeleton) or Alexa-647 labelled tubulin (PurSolutions). For rhodamine labelled microtubules, 20% of the tubulin was labelled, while Alexa-647 microtubules contained 33% labeled tubulin. This was accomplished by mixing 40 μl of unlabeled tubulin at 5 mg/ml in BRB-80 buffer (80 mM PIPES pH = 6.9, 1 mM $MgCl_2$, 1 mM EGTA) with 5% glycerol with 10 μl of either 2 mg/ml rhodamine tubulin in BRB-80 buffer or 10 mg/ml Alexa-647 tubulin in BRB-80 buffer. GTP was added to the tubulin mixture to a final concentration of 1 mM prior to incubation on ice for 5 minutes. The tubulin mixture was then clarified by ultracentrifugation at 392,000 x g for 10 minutes at 4° C, and the supernatant was transferred to a new tube. We optimized our polymerization protocol to generate the long MTs needed for this study. The tubulin mixture was incubated at 37° C in a water bath for 20 minutes, supplemented with 20 μM (final concentration) paclitaxel (Cytoskeleton) and further incubated for an additional 20 minutes at 37° C. After incubation, the tube containing the assembled MTs was wrapped in foil for storage in a dark drawer, thus minimizing potential photodamage. Polymerized MTs were stable at room temperature for up to one week.

*Single molecule quantum dot motility assays.*

On each experiment day, a kinesin aliquot was removed from -80° C storage and rapidly thawed before being placed in an ice bucket. The kinesin was brought to a final volume of 50 μl with ice cold Buffer 1 (25 mM Imidazole pH = 7.4, 300 mM KCl, 4 mM EGTA, 4 mM $MgCl_2$), transferred to a chilled ultracentrifuge tube, and clarified by ultracentrifugation at 392,000 x g for 10 minutes at 4° C. The clarified protein was transferred to a fresh tube on ice and diluted to a final concentration of 100 nM in Buffer 2 (25 mM Imidazole pH = 7.4, 25 mM KCl, 4 mM EGTA, 4 mM $MgCl_2$). To generate kinesin-Qdot complexes, we mixed 2 μl of 100 nM kinesin with 2 μl of 1 μM Qdot 655 Streptavidin Conjugate (ThermoFisher) and 6 μl Buffer 2 and incubated on ice for at least 1 hour. The 10:1 ratio of Qdots to kinesin was selected because Poisson statistics predict that less than 0.5% of the Qdots will be bound to more than 1 kinesin, ensuring that experiments are truly in single molecule conditions. These assays were performed identically for K543 (Bensel et al., 2024).

Single molecule experiments were performed on silanized cover glass. Pieces of 24x60 mm No. 1 cover glass were incubated in acetone for 1 hour, followed by incubation in ethanol for 10 minutes and two sequential washes in $ddH_2O$ for 5 minutes each. The cover glass was then incubated in 0.1 M KOH for 15 minutes followed by three sequential washes in $ddH_2O$ for 5 minutes each. The cover glass was then dried fully before incubation in PlusOne Repel-Silane ES (Cytiva) for 5 minutes, followed by two consecutive washes in ethanol for 5 minutes each, and three final washes in $ddH_2O$ for 5 minutes each. Motility chambers were prepared by attaching a 22x22 mm No. 1 cover glass to a silanized 24x60 mm silanized cover glass, separated by 125 μm Mylar shims, using UV-curable adhesive (Norland Optical Adhesive 68). The motility surface was prepared by first coating with 0.8% anti-tubulin antibody (BioRad YL1/2) in BRB-80 and incubating for 5 minutes. The chamber was then washed with Wash Buffer (BRB-80 plus 20 μM paclitaxel) prior to blocking with 5% w/v Pluronic F-127 in BRB-80

for an additional 5 minutes. After another wash with Wash Buffer, rhodamine-labelled MTs diluted 1:400 in BRB-80 with 20 μM paclitaxel were flowed into the motility chamber and incubated for 10 minutes prior to a final wash with Wash Buffer. Kinesin-Qdot complex was diluted 1:20 in Motility Buffer (Buffer 1 with 2 mM MgATP, 20 μM paclitaxel, 0.5 mg/ml Casein, 0.5% w/v Pluronic F-127, 5 mM creatine phosphate, 0.4 mg/ml creatine phosphokinase, 10 mM DTT, 3.5 mg/ml glucose, 40 μg/ml glucose oxidase, 27 μg/ml catalase) and flowed into the motility chamber. For experiments utilizing the kinesin activator Kinesore (Tocris Bioscence Cat. No. 6664), a Kinesore stock of 50 mM was prepared in DMSO and kept at -20° C. On the day of the experiment, Kinesore was thawed, diluted 1:10 in DMSO, and the resultant Kinesore dilution was further diluted 1:100 in Motility Buffer alongside a control buffer containing an equivalent volume of DMSO. Motility videos and still images of MTs were acquired using a custom-built dual-camera TIRF microscope (Nelson et al., 2014; Lombardo et al., 2017) with 532-nm excitation to image MTs and 639-nm excitation to image Qdots. Videos of Qdot motility were acquired at 10 frames per second.

*Data analysis:*

Qdot motility was analyzed by kymography. To do this, both the MT and Qdot images were opened in ImageJ (Schindelin et al., 2012). Using the segmented line tool, a MT was traced and the trace was duplicated to the Qdot video. A kymograph was then generated using the Multi Kymograph plugin for ImageJ with a width of 3 pixels. Example kymographs can be found in Fig. 3 and Fig. 4. The kymograph is a 2D representation of a movie, where the horizontal axis represents time and the vertical axis represents distance along the line from which the kymograph was generated – in this case, that line corresponds to a MT. Any fluorescent particle on the MT appears in the kymograph, either as a sloped line if that particle is being moved by a kinesin, or as a horizontal line if the particle is stuck in place. To characterize moving particles, a bounding box is drawn around sloped lines on the kymograph where the width (horizontal) of the box equals the duration of the event, the height of the box (vertical)

represents the distance traveled during the event, and the velocity of the particle equals the height of the box divided by the width of the box. For any run which reached the end of the MT, the run length and velocity were still recorded, but labeled as reaching the MT end. Run length and velocity data are plotted as dot plots with the median and upper and lower quartiles overlaid on the plot. To determine MT landing rates, the number of events seen on a single kymograph was divided by the product of the length of the MT in μm and the duration of the movie in minutes. For each condition of interest, multiple kymographs were analyzed from multiple independent videos, and a mean landing rate and standard deviation were determined based on the landing rate observed in each kymograph in each condition.

*Liposome and kinesin-liposome complex preparation.*

Liposomes used in this study were prepared identically to those described previously (Nelson et al., 2014; Lombardo et al., 2017, 2019; Bensel et al., 2024). Lipids are first mixed with the following composition (expressed as molar ratio): 84 parts DOPC (Avanti Polar Lipids), 5 parts PEG-ylated phospholipid (Avanti Polar Lipids), 5 parts MBP:PE (Avanti Polar Lipids), 5 parts cholesterol (Avanti Polar Lipids), and 1 part lipophilic fluorescent dye DiI or DiO (Thermo Fisher Scientific) in a borosilicate glass culture tube. The lipid mixture is then dried initially under nitrogen gas flow, with the drying process completed by centrifugation under vacuum (Rotovap;Eppendorf) prior to overnight rehydration of the lipids in 500 μl PBS (pH = 7.4). The rehydrated lipids can be unstuck from the sides of the glass tube by manual agitation and then resuspended prior to extrusion through a 1 μm pore diameter extrusion filter (T&T Scientific). The extruded liposomes are then incubated with 1 μM thiolated neutravidin (SH-NaV) overnight. Excess SH-NaV is then removed by pelleting the liposomes by ultracentrifugation (392,000 x g for 10 minutes) and resuspending the liposome pellet in 400 μl PBS (pH = 7.4) 3 times. The washed liposomes are then extruded through a 200 nm pore diameter extrusion filter (T&T Scientific) and stored at room temperature in a dark drawer for up to one week of experiments.

This liposome preparation yields 400 μl of liposomes at a final concentration of 10 nM. For fluorescence-based motor counting assays (see below), liposomes were prepared with the fluorescent dye omitted to ensure that no background fluorescence interfered with motor counting.

To prepare kinesin-liposome complexes, either KinΔC or K543 aliquots were thawed and clarified as described above and diluted in Buffer 1 to the desired concentration (250 nM to 1 μM) depending on the kinesin-liposome ratio required for the experiment. 4 μl of diluted kinesin is mixed with 16 μl of liposomes (10 nM) and 20 μl of Buffer 2, and the mixture is incubated on ice for at least one hour. During this incubation period, the C-terminal biotin on the kinesin binds strongly to the SH-NaV on the liposome surface, thus affixing the motor to the liposome. To estimate the average number of kinesins bound per liposome, either a KinΔC with YFP-KLCs or a K543 with an N-terminal YFP was clarified, diluted in Buffer 1 as described above (300 nM – 2.5 μM), and incubated with liposomes lacking fluorescent DiI for one hour on ice as described above. During this incubation, flow chambers were prepared as described above. 0.8% w/v anti-tubulin antibody (BioRad YL1/2) in BRB-80 was flowed into the flow chamber and incubated for 5 minutes and washed with Wash Buffer. MTs were prepared as described above with the single change of omitting fluorescently-labelled tubulin. Polymerized MTs were diluted 1:400 in BRB-80 with 20 μM paclitaxel, flowed into the flow chamber, and allowed to incubate for 10 minutes prior to washing the chamber with Wash Buffer. Preparing the flow chamber surface in this manner promotes landing of liposomes onto the surface because kinesin strongly binds MTs in the absence of free nucleotide. Therefore, the YFP-kinesin-liposome complexes prepared here are diluted 1:20 into Motility Buffer without ATP, phosphocreatine, or creatine phosphokinase, and were flowed into the flow chamber immediately prior to imaging by TIRF microscopy with 488-nm excitation on a Nikon N-STORM microscope system with a framerate of ~60 frames per second. A liposome landing event was characterized by a near-instantaneous jump in

fluorescence followed by a gradual decay over time as individual YFP molecules were photobleached, and monitoring the integrated YFP intensity over time for a single liposome spot generates a photobleaching transient for that liposome (Fig. S1A). Because the number of fluorescent molecules on each liposome is too large to allow for clear observation of individual photobleaching steps (Nelson et al., 2014), we used a statistical photobleaching technique developed by Nayak and Ruttenberg (Nayak and Rutenberg, 2011), which we have used and described the analysis routine for in detail previously (Nelson et al., 2014; Lombardo et al., 2017; Bensel et al., 2024). This technique relies on first collecting a large family of photobleaching transients (>50) for each kinesin-liposome stoichiometry. The family of transients corresponding to each condition is then used to generate an ensemble average photobleaching transient for that condition. Then the variance between each individual photobleaching transient and the ensemble average photobleaching transient was determined, and based on that variance ($\sigma_I$), the initial intensity ($I_0$), and the photobleaching rate (dp), the intensity per fluor (v) was determined with eq. 1 (Nayak and Rutenberg, 2011):

Eq. 1 $$v = 6\int_0^1 \frac{\sigma_I^2\, dp}{I_0}$$

Based on the intensity per fluor (v), the number of bound fluorescent molecules (n) in each transient could then be determined with eq. 2 (Nayak and Rutenberg, 2011):

Eq. 2 $$n = \frac{I_0}{v}$$

Dividing the number of bound fluorescent molecules (n) by 2 to account for the dimeric nature of kinesin yields an estimate of the number of bound kinesins for each liposome. By performing this analysis across a range of kinesin to liposome ratios, we generated a standard curve of the number of bound kinesins versus the kinesin to liposome ratio in the incubation tube (Fig. S1B and C).

*Multi-motor liposome motility assays and data analysis.*

To perform liposome motility assays, liposomes containing the fluorescent dye DiI were prepared over two days leading up to the experiment. On the day of the experiment, an aliquot of kinesin was thawed, brought to a final volume of 50 μl with Buffer 1, and clarified by ultracentrifugation. The resultant supernatant was placed in a fresh tube on ice and then diluted to the required concentration to achieve the kinesin-liposome ratio needed for the experiment. Then, 4 μl of diluted kinesin (concentration range 0.4 to 1.6 μM) was mixed with 16 μl of liposomes (10 nM) and 20 μl of Buffer 2 and set to incubate on ice for at least 1 hour. Motility chambers were prepared as described above for single molecule motility assays, with same order of reagents and incubation times. Immediately before imaging, liposomes were diluted 1:20 into Motility Buffer and were perfused into the motility chamber prior to imaging by TIRF microscopy on the same custom microscope described above with 532-nm excitation to image MTs and 639-nm excitation to image the DiI liposomes, and motility was recorded at a framerate of 10 frames per second.

*Data analysis:*

As in the single molecule motility experiments, liposome motility data were analyzed via kymography. Each run was identified with a bounding box where the height of the box gave the run length, the width of the box gave the event duration, and the height of the box divided by the width of the box gives the event velocity. Multi-motor runs were much more likely to reach the end of the MT, so end events were clearly marked in the analysis spreadsheet (Mayr et al., 2011; McKenney et al., 2014; Soppina et al., 2014). Run length and velocity data are shown as dot plots with overlaid median and upper and lower quartiles. End event frequences are shown as bar graphs.

*Optical trapping assays.*

We use 500-nm lipid-coated silica microspheres as model cargo for both single- and multi-motor trapping experiments as published previously (Lombardo et al., 2017; Bensel et al.,

2024), based on (Bayerl and Bloom, 1990; Mornet et al., 2005). First, liposomes are prepared containing fluorescent DiI dye as described above but are not extruded through the 200 nm diameter extrusion filter. Instead, the liposomes are washed 3 times by ultracentrifugation (392,000 x g for 10 minutes) to remove excess SH-NaV and resuspended in Buffer 3 (10 mM HEPES pH = 7.2 and 150 mM NaCl)) and brought up to a volume of 600 μl. The liposomes are then sonicated in an ice bath at low power with 0.5s alternating on/off pulses for a total sonication time of 10 minutes (total elapsed time is therefore 20 minutes). The liposomes are then centrifuged for 10 minutes at 5,000 x g to remove any metal shards from the sonicator probe, and the supernatant is transferred to a fresh tube. A 50 μl sample of 500 nm diameter silica microspheres (Duke Standard) was washed 3x with methanol and dried in a speedvac (Rotovap:Eppendorf) for 1 hour and then resuspended in 200 μl of Buffer 3. The sonicated liposomes were then incubated at 60° C for 2 minutes, mixed with the resuspended silica microspheres, and then immediately vortexed, briefly sonicated, and vortexed once again to promote adsorption of the lipids onto the surface of the silica microspheres. The microsphere and liposome mixture was then shaken for 1 hour at room temperature on a vortex mixer at low speed. To remove excess lipids, the lipid-coated microspheres were centrifuged at 5,000 x g for 3 minutes and resuspended in 200 ml of PBS (pH = 7.4) for a total of 3 repetitions prior to final resuspension in 200 ml of PBS (pH = 7.4) and storage at 4° C on a tube roller (BioRad) to keep the microspheres in suspension for up to 3 days.

On an experiment day, an aliquot of Kin∆C or K543 was thawed and clarified and diluted into Buffer 1 as described above. To perform multi-motor force assays, the kinesin was mixed with lipid-coated silica microspheres in a 20-fold molar excess, while single molecule force assays were performed with limiting kinesin. On each experiment day, single molecule conditions were verified by screening microspheres to find a kinesin concentration which yielded ~1 in every 10 lipid-coated beads generating force upon interaction with a MT. Kinesin and lipid-

coated silica microspheres were incubated on ice for at least 1 hour. During this incubation, flow cells were prepared. As in the experiments described above, a flow cell was assembled by attaching a 22x22 mm cover glass to a silanized 24x60 mm cover glass using a UV-curable adhesive and 125 μm mylar shims. The flow cell was first coated with 0.8% w/v anti-tubulin antibody (BioRad YL1/2) in chilled BRB-80 (pH = 7.2), incubated for 5 minutes, and washed with Wash Buffer. To block the flow cell surface, 1 mg/ml Casein (Sigma Aldrich Cat. No. C0406) in Buffer 2 was perfused into the chamber and incubated for 5 minutes, then washed with Wash Buffer. Rhodamine-labelled MTs were diluted 1:400 into BRB-80 (pH = 7.2) with 20 μM paclitaxel and flowed into the flow cell, incubated for 5 minutes, then flowed a second time, incubated for 5 additional minutes, and washed away with Wash Buffer. This strategy aligned the MTs with the long axis of the flow cell, which puts most of the resistive load of the trap along a single axis aligned with the MT. The final step in preparing the experiment chamber was to perfuse the chamber with Motility Buffer and add 2 μl of a 1:10 dilution of lipid-coated silica microspheres with kinesin in Motility buffer to one end of the flow cell. Doing this creates a "bead front" and makes it easier to trap a single lipid-coated silica microsphere at a time. For experiments performed with Kinesore, a Kinesore stock of 50 mM was prepared in DMSO and kept at -20° C. On the day of the experiment, Kinesore was thawed, diluted 1:10 in DMSO, and the resultant Kinesore dilution was further diluted 1:100 in Motility Buffer alongside a control buffer containing an equivalent volume of DMSO.

Optical trapping assays were performed on a commercially available optical trap (Lumicks C-Trap System) which is controlled using the supplied software, BlueLake (Lumicks). Once a lipid-coated silica microsphere was stably trapped, a power spectrum was collected to determine the trap stiffness. This was repeated for each lipid-coated silica microsphere as small variations in the trapped particle can lead to a different trap stiffness at any given laser power. The trap stiffness used throughout this study ranged from ~0.04 to 0.06 pN/nm. After calibration,

the trapped particle was manipulated until it was in close proximity to a rhodamine-labelled MT, and recordings of the force on that particle were collected. For Kin∆C ensemble ramp force control, 170 events from 9 beads over 3 bead preparations were collected, for Kin∆C single motor ramp force control, 108 events from 13 beads over 5 bead preparations were collected, and for Kin∆C in 50 μM Kinesore, 418 events from 10 beads over 3 bead preparations were collected.

*Data analysis:*

Force recordings from optical trapping assays were analyzed using a custom-written R script which performed several simple operations. First, a moving median force was calculated using a 12.5 ms time window. An event start was defined as the point at which this value rose to 1 pN above the baseline force of the event. The end of an event (i.e., detachment) is characterized by a single-step return to baseline force. To identify such events, a rolling difference along the force vector was calculated, and the time of detachment was defined as the local maximum of this rolling difference, and the detachment force for the given event was defined as the median force on the particle for the 50 ms immediately prior to detachment, and the event lifetime was simply defined as the time elapsed between the event start and detachment. Detachment force distributions were fit using the fitdistr function of the MASS packing in R (Venables and Ripley, 2002), using a single Gaussian for single motor experiments and a Gaussian mixture model for multi-motor experiments. Log-likelihood ratio testing was performed to determine if the inclusion of a third Gaussian was statistically justifiable (Venables and Ripley, 2002).

*3D MT intersection assay.*

Motility chambers with two perpendicular flow channels were assembled using a plasma-cleaned 48x60 mm No. 1 cover glass as a base, 4 square pieces of 125 μm mylar shims as vertical spacers, and a 22x22 mm No. 1 cover glass as a top, with UV-curable adhesive affixing

the assembly together (Lombardo et al., 2017, 2019; Bensel et al., 2024). Because 3D intersections must be suspended above the glass surface to allow for liposomes to have 360° access to the MTs, we use pedestal beads to raise the MTs away from the cover glass surface. Pedestal beads are generated in the lab using mixtures of silica microspheres (Duke Standard) with varying diameters between 1.0 and 3.0 μm. Prior to the experiment, the silica beads are coated with poly-L-lysine to promote binding of MTs to the bead surface rather than the cover glass surface. The silica microspheres are gently pelleted (3,000 x g for 2 minutes) and then resuspended in 400 μg/ml poly-L-lysine in 0.5 M TRIS Buffer (pH = 8.0) and incubated overnight at 4° C on a tube roller (BioRad) to keep the beads in suspension. This pedestal bead stock was able to be stored and used for up to 3 days. On the day of an experiment, a portion of the pedestal beads were removed from the stock, washed 3x with 1M TRIS (pH = 8.0) by pelleting at 3,000 x g for 2 minutes and resuspended in 1M TRIS (pH = 8.0) at a concentration of ~1% solids. The diluted pedestal beads were then perfused into a motility chamber with two perpendicular channels and rapidly washed 2x with 1M TRIS (pH = 8.0) and kept in a humid petri dish until just prior to imaging.

To prepare the motility chamber containing pedestal beads, both flow channels were first incubated with 1 mg/ml BSA in Buffer 2 for 5 minutes to block the surface and then washed with Wash Buffer. MTs labelled with Alexa-647 (PurSolutions) were prepared as described above and diluted 1:100 in BRB-80 buffer (pH = 7.2) supplemented with 20 μM paclitaxel. An alternating sequential flow approach was used to align MTs along the two perpendicular channels of the motility chamber, thus creating primarily perpendicular MT intersections. First, diluted MTs were perfused through one channel of the flow cell, incubated for 2 minutes, and then washed with Wash Buffer. This process was then repeated in the same channel of the flow cell. Next, diluted MTs were perfused through the perpendicular channel of the flow cell, incubated for 2 minutes, and then washed with Wash Buffer. This process was repeated a second time. Immediately

prior to imaging, both flow channels were perfused with STORM buffer (Buffer 2 supplemented with 20 μM paclitaxel, 50 mM beta-mercaptoethanol, and 20 mM Cysteamine). After the STORM image was acquired, both flow channels were washed with Motility Buffer. DiO-labelled fluorescent liposomes decorated with an average of 10 kinesins each were then diluted 1:100 in Motility Buffer and perfused into the flow cell and imaged.

Imaging was performed on a Nikon N-STORM microscope equipped with a precise piezoelectric stage and a cylindrical lens. The cylindrical lens introduces an astigmatism into the optical path which distorts the point spread function of an object based on the distance in Z from the object to the focal plane. Therefore, a calibration was performed by stepping the piezoelectric stage in Z, allowing us to use the shape of a point spread function to determine its vertical position relative to the focal plane (Huang et al., 2008; Henriques et al., 2010). STORM images of the suspended Alexa-647 MTs were collected by exciting with 405 and 647 nm light and collecting a stack of 20,000 images at a high (~60 Hz) framerate. Liposomes were imaged using 561 nm excitation at a framerate of 10 Hz. Because the pedestal beads were visible in both the 561 nm and 647 nm channels, they could be used as fiducial markers to align the two channels in the XY-plane, while the built in Nikon Perfect Focus system ensured that both image stacks were taken at identical Z heights.

*Data analysis:*

Super-resolution particle localizations for the STORM reconstruction of the MTs were performed using the DoM (Detection of Molecules) plugin for ImageJ (Katrukha et al., 2022), with 3D localizations accomplished by duplicating the Z-calibration curve from the Nikon software routine into DoM. Drift correction was performed using a cross-correlation based tool that is also built into DoM. High resolution tracking of liposomes was performed using DoM, and 3D localizations were also accomplished by duplicating the Z-calibration from the Nikon software routine into DoM. It is important to note that the calibration curves for each wavelength are slightly different, so it is crucial that the liposome and MT calibrations are selected correctly.

Liposome localizations were linked into tracks using the “Link Particles to Tracks” function built into DoM.

To analyze intersection outcomes and the spatial relationship of each liposome to the intersecting MTs, custom written R scripts were used (Bensel et al., 2024). First, the 3D STORM localizations for a given intersection ROI (region of interest) were imported into an R script which fit a 3D line segment to the point clouds defining each MT. A second R script overlaid the liposome trajectory onto the fitted line segments defining the intersecting MTs and determined the liposome outcome (straight, turn, terminate), the geometry of the liposome as it approached the intersection (i.e., angle of approach), the Z separation between the MTs at the point of intersection, and the angle between the intersecting MTs in the XY plane. Only intersections where the angle between the MTs was between 60° and 120° were included in the analysis. The calculation of the angle of liposome approach was performed as follows; first, the average Z position of the liposome over the 10 frames prior to it reaching the intersection was determined; second, the azimuthal angle between the liposome center and a vertical line passing through both MTs at the point of intersection was calculated, which is the angle of approach. Liposome pausing in 3D intersections was measured by kymography. In order for a pause to count, motion had to appear stalled in the kymograph for at least 3 frames.

*Size Exclusion Chromatography*

200 µg of 1.6 mg/ml mouse kinesin-ΔC with bound kinesin light chain was applied to a 10 x 300 mm Superose 6 (Amersham Biosciences) using an AKTA FPLC (Amersham Pharmacia Biotech). The column was equilibrated with BRB80 (80 mM Pipes pH 7.2, 1 mM EGTA, 1 mM $MgCl_2$, 1 mM dithiothreitol) and the protein eluted at a speed of 0.4 ml/min. Each 0.5 ml fraction was concentrated and the total amount in each fraction was applied to a Nupage 4-12% Bis-Tris SDS Gel (Invitrogen). The same experiment was repeated in the presence of 50 µM kinesore (50 mM stock in DMSO) (Tochris Bioscience) in the column equilibration and elution buffers.

*Mechanistic mathematical modeling.*

By design, the mathematical model used in this study is identical to the model we used to describe the shorter, constitutively active kinesin-1 construct K543 (Bensel et al., 2024). Furthermore, all parameters in the model were unchanged, save either the number of kinesin or the attachment rate as described in more detail below. Since the model successfully describes our observations of single motor run length, ensemble force generation in the laser trap, and outcomes of multi-motor liposome transport through microtubule intersections with K543 (Bensel et al., 2024) -- the same experiments performed here with Kin∆C -- this approach allows us to determine whether our current observations can be satisfactorily explained by the three-fold reduction in attachment rate we observed in the landing assay (see Results and Discussion).

*Modeling details*

Our modeling approach is similar to previously published models (Hendricks et al., 2009; Kunwar and Mogilner, 2010; Bergman et al., 2018; Bovyn et al., 2021; Sarpangala and Gopinathan, 2022; D'Souza et al., 2023). In particular, we use a physical model of the various system components (liposome, motors, microtubules) and model their dynamics with a Brownian dynamics simulation implemented with the Euler-Maruyama method. Kinesin motors, when attached to a microtubule, step according to a modified version of the three-state model proposed by Andreasson et al. (Andreasson et al., 2015) that accounts for the effects of external force on reaction rates. We modify the model slightly to allow backsteps, rare side-steps, and to fit our run length measurements with K543 (Bensel et al., 2024). Chemical reactions are implemented with a constant time step, which is 20-fold larger than the time step for the Euler-Maruyama time step. We describe these aspects of the model in more detail below; additional details and justification can be found in Bensel et al. 2024.

*Physical model of system components:* Each kinesin molecule is a rigid rod of length 25nm attached to the liposome surface by a ball joint. This attachment occurs via a linear-elastic linkage with zero rest length and stiffness 1pN/nm. The attachment point diffuses on the surface

of the liposome, and can also slide across the surface of the liposome with a viscous drag ($\gamma_K$) that is related to the diffusion constant ($D_K$) via the Einstein-Smoluchowski relation $D_K = k_B T/\gamma_K$, with $k_B T$ being Boltzmann's constant times temperature. The liposome is a rigid sphere of diameter 350nm (or 500nm in the laser trap simulations). Each microtubule is a rigid rod of diameter 25nm. Collisions between the liposome and microtubles are perfectly elastic; collisions involving kinesin molecules and 1) other kinesin molecules, 2) microtubules, 3) the liposome, are neglected.

*Equations of motion:* We model the Brownian dynamics of the system in three-dimensions (3D) using a Langevin equation for the liposome's position in 3D, $\vec{x}_L$:

Eq. 3 $$\vec{x}_L(t+\Delta t) = \vec{x}_L(t) + \frac{\Delta t}{\gamma_L}\sum_{i=1}^{N_B}\vec{F}_i + \vec{w}_f$$

where $\vec{F}_i$ is the force applied by the *i*$^{th}$ bound kinesin molecule on the liposome, $\gamma_L$ is the viscous drag constant of the liposome, $N_B$ is the number of kinesin motors bound to the microtubule(s), and $\vec{w}_f$ is a Gaussian distributed random variable with mean 0 and standard deviation $\sqrt{2D_L\Delta t}$, were $D_L$ is the diffusion constant of the liposome, to capture Brownian fluctuations of the liposome due to solvent collisions. A similar Langevin equation describes the 3D orientation of the liposome, $\vec{\theta}_L$:

Eq. 4 $$\vec{\theta}_L(t+\Delta t) = \vec{\theta}_L(t) + \frac{\Delta t}{\gamma_\theta}\sum_{i=1}^{N_B}\vec{M}_i + \vec{\phi}_f$$

where $\vec{M}_i$ is the moment applied by the *i*$^{th}$ bound kinesin molecule on the liposome, $\gamma_\theta$is the angular viscous drag constant of the liposome, and $\vec{\phi}_f$ is a Gaussian distributed random variable with mean 0 and standard deviation $\sqrt{2D_\theta\Delta t}$, where $D_\theta$ is the angular diffusion constant of the liposome, to capture Brownian fluctuations of the liposome due to solvent collisions. The position $\vec{x}_K$ of each kinesin molecule diffusing over the surface of the liposome obeys a 2D Langevin equation:

Eq. 5 $$\vec{x}_K(t+\Delta t) = \vec{x}_K(t) + \frac{\Delta t}{\gamma_K}\left((\vec{F}\cdot\hat{e}_{t1})\hat{e}_{t1} + (\vec{F}\cdot\hat{e}_{t2})\hat{e}_{t2}\right) + w_1\hat{e}_{t1} + w_2\hat{e}_{t2}$$

where $\vec{F}$ is the force on the kinesin, $w_1$and $w_2$ are Gaussian distributed random variables with mean 0 and standard deviation $\sqrt{2D_K\Delta t}$ to capture Brownian fluctuations of the kinesin due to solvent collisions, and the two unit vectors $\hat{e}_{t1}$ and $\hat{e}_{t2}$ are any two orthogonal vectors tangent to the liposome surface that originate from where the kinesin attaches to the liposome. After calculating $\vec{x}_K(t+\Delta t)$, we project back onto the surface of the liposome to eliminate the small error associate with the fact that the two unit vectors $\hat{e}_{t1}$ and $\hat{e}_{t2}$ are straight while the liposome surface is curved.

*Diffusion constants and drag:* As previously mentioned for kinesin, the viscous drag of the liposome is related to the diffusion constant by the Einstein-Smoluchowski relation $D = k_B T/\gamma$. For the liposome, we assume Stokes drag $\gamma_L = 6\eta\pi r_L$ where $\eta$ is the dynamic viscosity of water at 25C, and $r_L$ is the radius of the liposome. This assumption also allows us to calculate the angular drag $\gamma_\theta = 8\pi\eta r_L^3$. The diffusion constant for kinesin on the liposome surface comes from experimental measurements (Nelson et al., 2014).

*Kinesin attachment:* Each microtubule is assumed to have 13 protofilaments and a 3-start geometry. The kinesin binding sites are arrayed every 8nm along these protofilaments, and are positioned at the microtubule surface, 12.5nm from the center of the microtubule. When kinesin binds to one of these binding sites, we assume it is oriented normal to the microtubule surface. The binding rate of a given kinesin molecule to a given binding site is assumed to be exponentially related to the energy difference between the free and the bound state

Eq. 6 $$k_a = k_{a,0}\, exp\left(-\frac{\kappa(\vec{x}_K - \vec{x}_{tail})^2}{2k_B T}\right)$$

where $\vec{x}_K$ is the point where kinesin attaches to the liposome, $\vec{x}_{tail}$ is the position of kinesin's tail were it to bind to the binding site, $\kappa$ is kinesin's stiffness, and $k_{a,0}$ is the maximal binding rate.

*Numerical implementation:* The equations of motion provide a method to step the kinesin-liposome-microtubule system forward in time. Given an initial configuration of this system and a time step, we can apply these steps repeatedly to obtain position-time traces of all

of the system components. We choose a small time step, $\Delta t = 5 \times 10^{-7}$s, so that the length scale of the diffusion step ($\sqrt{2D_L\Delta t}$) is on the same order as the length scale of the attachment zone ($\sqrt{k_B T/\kappa}$). As mentioned previously, we use a larger time step for our constant step-size implementation of chemical reactions, $\Delta t_c = 1 \times 10^{-5}$s, both to reduce the computational cost of the simulations and to minimize the effects of round-off error. All simulations were performed on a standard laptop.

*Initial conditions:* Each simulation started with a single kinesin molecule bound to a microtubule. The remaining kinesin molecules then diffused on the liposome surface for 0.002s and, during that time, were not allowed to bind to the microtubule. In this way, the kinesin molecules were spread randomly over the surface of the liposome.

**Simulating the different experiments**

All simulations were performed as described above. However, there were some differences between simulations of individual experiments. These are motivated and explained more fully in Bensel et al., 2024.

*Single microtubule:* Simulations started as described above and continued until either all kinesin detached from the microtubule or the time in the simulation reached 15s (30 million time steps). Since the liposomes often reached the end of the microtubule in experiments, we estimated the distribution of distances to the end of the microtubules in our measurements (Bensel et al., 2024). We randomly drew a microtubule length from this distribution, and if the simulated run length was longer than this length we assumed that run length was limited by the microtubule. Otherwise, we assumed that detachment from the microtubule limited the run length.

*Laser trap:* Experiments were performed with 500nm-diameter beads, so we adjusted the liposome size to 500nm. Simulations started as described above and continued until either all kinesin detached from the microtubule or the time in the simulation reached 15s (30 million

time steps). No simulations reached 15s. The laser trap was modeled as a force on the center of the liposome, directed toward the microtubule minus end, and proportional to the distance traveled, $d_T$: $F = -k_{trap} d_T$. In the simulations, the stiffness of the laser trap was set to $k_{trap} =$ 0.04pN/nm.

*Microtubule intersections:* At the start of each simulation, a single kinesin motor was engaged with the "starting" microtubule and the second, the "crossing" microtubule, was positioned 1.6μm toward the plus end of the starting microtubule, and oriented perpendicular to it. The crossing microtubule was positioned 40, 50, 75, 100, 125, or 150nm above the starting microtubule. Simulations proceeded until either all kinesin detached from the microtubule, the center of the liposome passed 4 liposome diameters past the intersection, or the time in the simulation reached 15s (30 million time steps). No simulations reached this maximum time.
For each spacing, we ran 10 simulations with the initially bound kinesin on the top of the starting microtubule (initial angle of 0) and 10 simulations with the initially bound kinesin on the side (initial angle +/-90 degrees, choosing each sign with equal probability). Simulations where the motors detached prior to the intersection were not included in the analysis. The remaining simulations were scored as a turn outcome if the cargo continued 1 diameter past the intersection on the crossing microtubule, a straight outcome if the cargo continued 1 diameter past the intersection on the starting microtubule, a terminate outcome if all kinesin detached from the microtubules while the cargo was within 1 diameter of the intersection.
To determine the approach angle α, we used the equation $\alpha = \mathrm{acos}(\overline{z_L}/r_{eff})$, where $r_{eff} =$ $182.5$nm was the effective radius of the liposome-kinesin system, and $\overline{z_L}$is the height of the liposome averaged over 0.6s before it reached the intersection (i.e., the center of the liposome was within 212.5nm of the center of the crossing microtubule).

*Force dependence:* The literature value for the force-dependence of unbinding under resistive loads is 1.1nm (Andreasson et al., 2015). We used 0.7nm in the intersection and single

microtubule simulations, and 0.9nm in the laser trap simulations. These modifications aim to account for the fact that vertical loads likely occur in the laser trap (Bensel et al., 2024; Pyrpassopoulos et al., 2022).

**Modifications for KinΔC**

We performed two sets of simulations. In the first set, we performed the above described simulations with N=3 and then again with N=4 (single microtubule, microtubule intersections) and with N=7 (laser trap). This approach allowed us to investigate whether our experimental observations with KinΔC could be explained by a 3-fold reduction in motor number with respect to our observations the K543, since we can explain these latter observations with the model having N=10 kinesin motors in the single microtubule and microtubule intersection measurements, and N=20 kinesin motors in the laser trap (Bensel et al., 2024). In the second set of simulations, we performed the above described simulations with a 3-fold reduction in attachment rate, $k_{a,0} = 50\text{s}^{-1}$, compared to the model that successfully described our observations with K543 which used $k_{a,0} = 150\text{s}^{-1}$.

**Data availability statement**

Due to the size of the super resolution imaging datasets, data are stored on University of Vermont servers. The data are available from the corresponding author upon reasonable request.

**Acknowledgements**

We would like to acknowledge Shane R. Nelson for supporting in developing data analysis scripts, M. Yusuf Ali for experimental input, Guy Kennedy for TIRF microscopy support and training, Andrew Lombardo for guidance on experiments and data analysis, Douglas Taatjes and Nicole Bouffard of the UVM Microscopy Imaging Center (RRED# SRC_018821) for training and

support in 3D N-STORM imaging and analysis. We would also like to thank current and former members of the Warshaw and Trybus labs for their invaluable input, discussions, and support. The work published here would not have been possible without the contributions of those who have played a role in the creation, distribution, and maintenance of the open-source software packages used in this study, particularly r-project.org and ImageJ.nih.gov. We also thank our funding: NIH Grant T32HL076122 (to B.M.B.), NIH Grant F32GM140618 (to B.M.B.), NIH Grant R35GM141743 (to D.M.W.), NIH Grant R35GM136288 (to K.M.T.), and NIH Grant S10OD026884 (to D.M.W.), and a generous gift from Arnold and Mariel Goran to D.M.W.

**References**

Ali, M.Y., H. Lu, C.S. Bookwalter, D.M. Warshaw, and K.M. Trybus. 2008. Myosin V and Kinesin act as tethers to enhance each others' processivity. *Proc. Natl. Acad. Sci. U.S.A.* 105:4691–4696. doi:10.1073/pnas.0711531105.

Andreasson, J.O.L., S. Shastry, W.O. Hancock, and S.M. Block. 2015. The Mechanochemical Cycle of Mammalian Kinesin-2 KIF3A/B under Load. *Current Biology*. 25:1166–1175. doi:10.1016/j.cub.2015.03.013.

Angerani, S., E. Lindberg, N. Klena, C.K.E. Bleck, C. Aumeier, and N. Winssinger. 2021. Kinesin-1 activity recorded in living cells with a precipitating dye. *Nat Commun*. 12:1463. doi:10.1038/s41467-021-21626-1.

Bálint, Š., I. Verdeny Vilanova, Á. Sandoval Álvarez, and M. Lakadamyali. 2013. Correlative live-cell and superresolution microscopy reveals cargo transport dynamics at microtubule intersections. *Proc. Natl. Acad. Sci. U.S.A.* 110:3375–3380. doi:10.1073/pnas.1219206110.

Barlan, K., and V.I. Gelfand. 2017. Microtubule-Based Transport and the Distribution, Tethering, and Organization of Organelles. *Cold Spring Harb Perspect Biol*. 9:a025817. doi:10.1101/cshperspect.a025817.

Bayerl, T.M., and M. Bloom. 1990. Physical properties of single phospholipid bilayers adsorbed to micro glass beads. A new vesicular model system studied by 2H-nuclear magnetic resonance. *Biophysical Journal*. 58:357–362. doi:10.1016/S0006-3495(90)82382-1.

Bensel, B.M., S.B. Previs, C. Bookwalter, K.M. Trybus, S. Walcott, and D.M. Warshaw. 2024. Kinesin-1-transported liposomes prefer to go straight in 3D microtubule intersections by a mechanism shared by other molecular motors. *Proc. Natl. Acad. Sci. U.S.A.* 121:e2407330121. doi:10.1073/pnas.2407330121.

Bergman, J.P., M.J. Bovyn, F.F. Doval, A. Sharma, M.V. Gudheti, S.P. Gross, J.F. Allard, and M.D. Vershinin. 2018. Cargo navigation across 3D microtubule intersections. *Proc. Natl. Acad. Sci. U.S.A.* 115:537–542. doi:10.1073/pnas.1707936115.

Bovyn, M., B.R. Janakaloti Narayanareddy, S. Gross, and J. Allard. 2021. Diffusion of kinesin motors on cargo can enhance binding and run lengths during intracellular transport. *MBoC*. 32:984–994. doi:10.1091/mbc.E20-10-0658.

Cai, D., A.D. Hoppe, J.A. Swanson, and K.J. Verhey. 2007. Kinesin-1 structural organization and conformational changes revealed by FRET stoichiometry in live cells. *The Journal of Cell Biology*. 176:51–63. doi:10.1083/jcb.200605097.

Carrington, G., U. Fatima, I. Caramujo, T. Lewis, D. Casas-Mao, and M. Peckham. 2024. A multiscale approach reveals the molecular architecture of the autoinhibited kinesin KIF5A. *J Biol Chem*. 300:105713. doi:10.1016/j.jbc.2024.105713.

Chiba, K., K.M. Ori-McKenney, S. Niwa, and R.J. McKenney. 2022. Synergistic autoinhibition and activation mechanisms control kinesin-1 motor activity. *Cell Reports*. 39:110900. doi:10.1016/j.celrep.2022.110900.

Coy, D.L., W.O. Hancock, M. Wagenbach, and J. Howard. 1999. Kinesin's tail domain is an inhibitory regulator of the motor domain. *Nat Cell Biol*. 1:288–292. doi:10.1038/13001.

Cronan, J.E. 1990. Biotination of proteins in vivo. A post-translational modification to label, purify, and study proteins. *J Biol Chem*. 265:10327–10333.

D'Souza, A.I., R. Grover, G.A. Monzon, L. Santen, and S. Diez. 2023. Vesicles driven by dynein and kinesin exhibit directional reversals without regulators. *Nat Commun*. 14:7532. doi:10.1038/s41467-023-42605-8.

Feng, Q., K.J. Mickolajczyk, G.-Y. Chen, and W.O. Hancock. 2018. Motor Reattachment Kinetics Play a Dominant Role in Multimotor-Driven Cargo Transport. *Biophysical Journal*. 114:400–409. doi:10.1016/j.bpj.2017.11.016.

Ferro, L.S., Q. Fang, L. Eshun-Wilson, J. Fernandes, A. Jack, D.P. Farrell, M. Golcuk, T. Huijben, K. Costa, M. Gur, F. DiMaio, E. Nogales, and A. Yildiz. 2022. Structural and functional insight into regulation of kinesin-1 by microtubule-associated protein MAP7. *Science*. 375:326–331. doi:10.1126/science.abf6154.

Fourriere, L., A.J. Jimenez, F. Perez, and G. Boncompain. 2020. The role of microtubules in secretory protein transport. *Journal of Cell Science*. 133:jcs237016. doi:10.1242/jcs.237016.

Friedman, D.S., and R.D. Vale. 1999. Single-molecule analysis of kinesin motility reveals regulation by the cargo-binding tail domain. *Nat Cell Biol*. 1:293–297. doi:10.1038/13008.

Fu, M., and E.L.F. Holzbaur. 2014. Integrated regulation of motor-driven organelle transport by scaffolding proteins. *Trends in Cell Biology*. 24:564–574. doi:10.1016/j.tcb.2014.05.002.

Furuta, K., A. Furuta, Y.Y. Toyoshima, M. Amino, K. Oiwa, and H. Kojima. 2013. Measuring collective transport by defined numbers of processive and nonprocessive kinesin motors. *Proc. Natl. Acad. Sci. U.S.A.* 110:501–506. doi:10.1073/pnas.1201390110.

Gicking, A.M., T.-C. Ma, Q. Feng, R. Jiang, S. Badieyan, M.A. Cianfrocco, and W.O. Hancock. 2022. Kinesin-1, -2, and -3 motors use family-specific mechanochemical strategies to effectively compete with dynein during bidirectional transport. *eLife*. 11:e82228. doi:10.7554/eLife.82228.

Gilbert, S.P., S. Guzik-Lendrum, and I. Rayment. 2018. Kinesin-2 motors: Kinetics and biophysics. *Journal of Biological Chemistry*. 293:4510–4518. doi:10.1074/jbc.R117.001324.

Gross, S.P., M. Vershinin, and G.T. Shubeita. 2007. Cargo Transport: Two Motors Are Sometimes Better Than One. *Current Biology*. 17:R478–R486. doi:10.1016/j.cub.2007.04.025.

Heaslip, A.T., S.R. Nelson, A.T. Lombardo, S. Beck Previs, J. Armstrong, and D.M. Warshaw. 2014. Cytoskeletal Dependence of Insulin Granule Movement Dynamics in INS-1 Beta-Cells in Response to Glucose. *PLoS ONE*. 9:e109082. doi:10.1371/journal.pone.0109082.

Hendricks, A.G., B.I. Epureanu, and E. Meyhöfer. 2009. Collective dynamics of kinesin. *Phys. Rev. E*. 79:031929. doi:10.1103/PhysRevE.79.031929.

Hendricks, A.G., E.L.F. Holzbaur, and Y.E. Goldman. 2012. Force measurements on cargoes in living cells reveal collective dynamics of microtubule motors. *Proc. Natl. Acad. Sci. U.S.A.* 109:18447–18452. doi:10.1073/pnas.1215462109.

Henriques, R., M. Lelek, E.F. Fornasiero, F. Valtorta, C. Zimmer, and M.M. Mhlanga. 2010. QuickPALM: 3D real-time photoactivation nanoscopy image processing in ImageJ. *Nat Methods*. 7:339–340. doi:10.1038/nmeth0510-339.

Hirokawa, N., Y. Noda, Y. Tanaka, and S. Niwa. 2009. Kinesin superfamily motor proteins and intracellular transport. *Nat Rev Mol Cell Biol*. 10:682–696. doi:10.1038/nrm2774.

Hirokawa, N., and Y. Tanaka. 2015. Kinesin superfamily proteins (KIFs): Various functions and their relevance for important phenomena in life and diseases. *Experimental Cell Research*. 334:16–25. doi:10.1016/j.yexcr.2015.02.016.

Huang, B., W. Wang, M. Bates, and X. Zhuang. 2008. Three-Dimensional Super-Resolution Imaging by Stochastic Optical Reconstruction Microscopy. *Science*. 319:810–813. doi:10.1126/science.1153529.

Jamison, D.K., J.W. Driver, A.R. Rogers, P.E. Constantinou, and M.R. Diehl. 2010. Two Kinesins Transport Cargo Primarily via the Action of One Motor: Implications for Intracellular Transport. *Biophysical Journal*. 99:2967–2977. doi:10.1016/j.bpj.2010.08.025.

Katrukha, E., Jalmar Teeuw, Bmccloin, and J.D. Braber. 2022. ekatrukha/DoM_Utrecht: Detection of Molecules 1.2.5. doi:10.5281/ZENODO.7326569.

Kunwar, A., and A. Mogilner. 2010. Robust transport by multiple motors with nonlinear force–velocity relations and stochastic load sharing. *Phys. Biol.* 7:016012. doi:10.1088/1478-3975/7/1/016012.

Lakadamyali, M. 2014. Navigating the cell: how motors overcome roadblocks and traffic jams to efficiently transport cargo. *Phys. Chem. Chem. Phys.* 16:5907. doi:10.1039/c3cp55271c.

Lombardo, A.T., S.R. Nelson, M.Y. Ali, G.G. Kennedy, K.M. Trybus, S. Walcott, and D.M. Warshaw. 2017. Myosin Va molecular motors manoeuvre liposome cargo through suspended actin filament intersections in vitro. *Nat Commun*. 8:15692. doi:10.1038/ncomms15692.

Lombardo, A.T., S.R. Nelson, G.G. Kennedy, K.M. Trybus, S. Walcott, and D.M. Warshaw. 2019. Myosin Va transport of liposomes in three-dimensional actin networks is modulated by actin

filament density, position, and polarity. *Proc. Natl. Acad. Sci. U.S.A.* 116:8326–8335. doi:10.1073/pnas.1901176116.

Lu, H., M.Y. Ali, C.S. Bookwalter, D.M. Warshaw, and K.M. Trybus. 2009. Diffusive Movement of Processive Kinesin-1 on Microtubules. *Traffic*. 10:1429–1438. doi:10.1111/j.1600-0854.2009.00964.x.

Mayr, M.I., M. Storch, J. Howard, and T.U. Mayer. 2011. A Non-Motor Microtubule Binding Site Is Essential for the High Processivity and Mitotic Function of Kinesin-8 Kif18A. *PLoS ONE*. 6:e27471. doi:10.1371/journal.pone.0027471.

McKenney, R.J., W. Huynh, M.E. Tanenbaum, G. Bhabha, and R.D. Vale. 2014. Activation of cytoplasmic dynein motility by dynactin-cargo adapter complexes. *Science*. 345:337–341. doi:10.1126/science.1254198.

Monroy, B.Y., T.C. Tan, J.M. Oclaman, J.S. Han, S. Simó, S. Niwa, D.W. Nowakowski, R.J. McKenney, and K.M. Ori-McKenney. 2020. A Combinatorial MAP Code Dictates Polarized Microtubule Transport. *Developmental Cell*. 53:60-72.e4. doi:10.1016/j.devcel.2020.01.029.

Mornet, S., O. Lambert, E. Duguet, and A. Brisson. 2005. The Formation of Supported Lipid Bilayers on Silica Nanoparticles Revealed by Cryoelectron Microscopy. *Nano Lett.* 5:281–285. doi:10.1021/nl048153y.

Nayak, C.R., and A.D. Rutenberg. 2011. Quantification of Fluorophore Copy Number from Intrinsic Fluctuations during Fluorescence Photobleaching. *Biophysical Journal*. 101:2284–2293. doi:10.1016/j.bpj.2011.09.032.

Nelson, S.R., K.M. Trybus, and D.M. Warshaw. 2014. Motor coupling through lipid membranes enhances transport velocities for ensembles of myosin Va. *Proc. Natl. Acad. Sci. U.S.A.* 111. doi:10.1073/pnas.1406535111.

Osunbayo, O., J. Butterfield, J. Bergman, L. Mershon, V. Rodionov, and M. Vershinin. 2015. Cargo Transport at Microtubule Crossings: Evidence for Prolonged Tug-of-War between Kinesin Motors. *Biophysical Journal*. 108:1480–1483. doi:10.1016/j.bpj.2015.02.016.

Pyrpassopoulos, S., H. Shuman, and E.M. Ostap. 2022. Modulation of Kinesin's Load-Bearing Capacity by Force Geometry and the Microtubule Track. *Biophysical Journal*. 121:4748. doi:10.1016/j.bpj.2022.11.2939.

Randall, T.S., Y.Y. Yip, D.J. Wallock-Richards, K. Pfisterer, A. Sanger, W. Ficek, R.A. Steiner, A.J. Beavil, M. Parsons, and M.P. Dodding. 2017. A small-molecule activator of kinesin-1 drives remodeling of the microtubule network. *Proc Natl Acad Sci U S A*. 114:13738–13743. doi:10.1073/pnas.1715115115.

Reilein, A.R., S.L. Rogers, M.C. Tuma, and V.I. Gelfand. 2001. Regulation of molecular motor proteins. *In* International Review of Cytology. Elsevier. 179–238.

Rogers, A.R., J.W. Driver, P.E. Constantinou, D. Kenneth Jamison, and M.R. Diehl. 2009. Negative interference dominates collective transport of kinesin motors in the absence of load. *Phys. Chem. Chem. Phys.* 11:4882. doi:10.1039/b900964g.

Ross, J.L., M.Y. Ali, and D.M. Warshaw. 2008. Cargo transport: molecular motors navigate a complex cytoskeleton. *Current Opinion in Cell Biology*. 20:41–47. doi:10.1016/j.ceb.2007.11.006.

Sarpangala, N., and A. Gopinathan. 2022. Cargo surface fluidity can reduce inter-motor mechanical interference, promote load-sharing and enhance processivity in teams of molecular motors. *PLoS Comput Biol*. 18:e1010217. doi:10.1371/journal.pcbi.1010217.

Schindelin, J., I. Arganda-Carreras, E. Frise, V. Kaynig, M. Longair, T. Pietzsch, S. Preibisch, C. Rueden, S. Saalfeld, B. Schmid, J.-Y. Tinevez, D.J. White, V. Hartenstein, K. Eliceiri, P. Tomancak, and A. Cardona. 2012. Fiji: an open-source platform for biological-image analysis. *Nat Methods*. 9:676–682. doi:10.1038/nmeth.2019.

Schnitzer, M.J., K. Visscher, and S.M. Block. 2000. Force production by single kinesin motors. *Nat Cell Biol*. 2:718–723. doi:10.1038/35036345.

Schroeder, H.W., A.G. Hendricks, K. Ikeda, H. Shuman, V. Rodionov, M. Ikebe, Y.E. Goldman, and E.L.F. Holzbaur. 2012. Force-Dependent Detachment of Kinesin-2 Biases Track Switching

at Cytoskeletal Filament Intersections. *Biophysical Journal*. 103:48–58. doi:10.1016/j.bpj.2012.05.037.

Soppina, V., S.R. Norris, A.S. Dizaji, M. Kortus, S. Veatch, M. Peckham, and K.J. Verhey. 2014. Dimerization of mammalian kinesin-3 motors results in superprocessive motion. *Proc. Natl. Acad. Sci. U.S.A.* 111:5562–5567. doi:10.1073/pnas.1400759111.

Soppina, V., and K.J. Verhey. 2014. The family-specific K-loop influences the microtubule on-rate but not the superprocessivity of kinesin-3 motors. *MBoC*. 25:2161–2170. doi:10.1091/mbc.e14-01-0696.

Tan, Z., Y. Yue, F. Leprevost, S. Haynes, V. Basrur, A.I. Nesvizhskii, K.J. Verhey, and M.A. Cianfrocco. 2023. Autoinhibited kinesin-1 adopts a hierarchical folding pattern. *eLife*. 12:RP86776. doi:10.7554/eLife.86776.3.

Vale, R., T. Reese, and M. Sheetz. 1985. Identification of a novel force-generating protein, kinesin, involved in microtubule-based motility. *Cell*. 42:39–50. doi:10.1016/S0092-8674(85)80099-4.

Vale, R.D. 2003. The Molecular Motor Toolbox for Intracellular Transport. *Cell*. 112:467–480. doi:10.1016/S0092-8674(03)00111-9.

Venables, W.N., and B.D. Ripley. 2002. Modern Applied Statistics with S. Fourth. Springer, New York.

Verdeny-Vilanova, I., F. Wehnekamp, N. Mohan, Á.S. Álvarez, J.S. Borbely, J.J. Otterstrom, D.C. Lamb, and M. Lakadamyali. 2017. 3D motion of vesicles along microtubules helps them to circumvent obstacles in cells. *Journal of Cell Science*. jcs.201178. doi:10.1242/jcs.201178.

Verhey, K.J., and J.W. Hammond. 2009. Traffic control: regulation of kinesin motors. *Nat Rev Mol Cell Biol*. 10:765–777. doi:10.1038/nrm2782.

Verhey, K.J., N. Kaul, and V. Soppina. 2011. Kinesin Assembly and Movement in Cells. *Annu. Rev. Biophys.* 40:267–288. doi:10.1146/annurev-biophys-042910-155310.

Vershinin, M., B.C. Carter, D.S. Razafsky, S.J. King, and S.P. Gross. 2007. Multiple-motor based transport and its regulation by Tau. *Proc. Natl. Acad. Sci. U.S.A.* 104:87–92. doi:10.1073/pnas.0607919104.

Visscher, K., M.J. Schnitzer, and S.M. Block. 1999. Single kinesin molecules studied with a molecular force clamp. *Nature*. 400:184–189. doi:10.1038/22146.

Weijman, J.F., S.K.N. Yadav, K.J. Surridge, J.A. Cross, U. Borucu, J. Mantell, D.N. Woolfson, C. Schaffitzel, and M.P. Dodding. 2022. Molecular architecture of the autoinhibited kinesin-1 lambda particle. *Sci. Adv.* 8:eabp9660. doi:10.1126/sciadv.abp9660.

**Abbreviations**

2D: 2-dimensional

3D: 3-dimensional

K543: kinesin 543

Kin∆C: kinesin-∆C

KHC: Kinesin heavy chain

KLC: Kinesin light chain

MT: Microtubule

Qdot: Quantum dot

ROI: Region of interest

STORM: Stochastic optical reconstruction microscopy

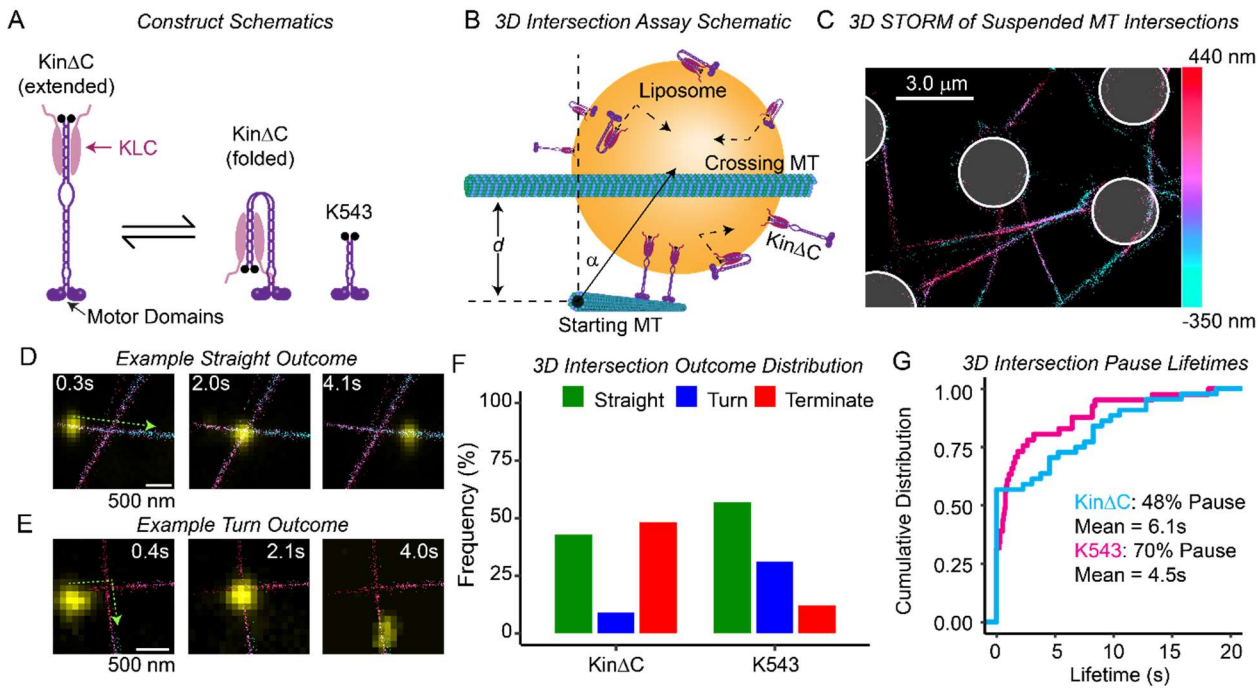


Figure 1. *KinΔC terminates frequently in 3D MT intersections.* (A) Schematic of constructs of interest. KinΔC (left) contains aa1-888 of murine KIF5B and copurifies with full-length KLC2. Critically, KinΔC is able to adopt the folded conformation associated with autoinhibition. K543 contains aa1-543 of murine KIF5B and serves as a constitutively active control. Both constructs are C-terminally biotinylated (black circles). (B) Schematic cartoon of 3D MT intersection assay. Liposome (gold) is transported by KinΔC (purple) along MTs (green) while KinΔC motors can diffuse on the liposome surface. The liposome is moving out of the page and approaches the horizontal MT in a 3D intersection. The geometry of the interaction between the liposome and the intersection is described by two parameters, *d* and $\alpha$, illustrated here, where *d* is the vertical gap between the intersecting MTs, and $\alpha$ is the angle of approach of the liposome coming in to the intersection, where an $\alpha$ of 0° indicates the liposome is pointed up towards the crossing MT, and an $\alpha$ of 180° indicates the liposome is pointed down and away from the crossing MT. (C) 3D STORM reconstruction of suspended MT intersections. Z-position of MTs is shown via the color bar on the right. (D) Example of a liposome (yellow) passing straight through a 3D intersection.

Color bar as in C. Gap = 34 nm. (E) Example of a liposome (yellow) turning in a 3D intersection. Color bar as in C. Gap = 174 nm. (F) Bar graph of 3D intersection outcomes for liposomes with 10 Kin∆C (left) compared to 10 K543 control (right). 10 K543 control data are replotted from Bensel et al., 2024. For Kin∆C data, N = 57 intersection outcomes from 3 independently performed intersection assays. (G) Cumulative distribution plot of the pause lifetimes observed for liposomes with 10 Kin∆C (cyan) and 10 K543 (magenta) in 3D intersections. Events with no discernible pause are represented as a pause lifetime of 0s. K543 lifetime data are replotted from Bensel et al., 2024.

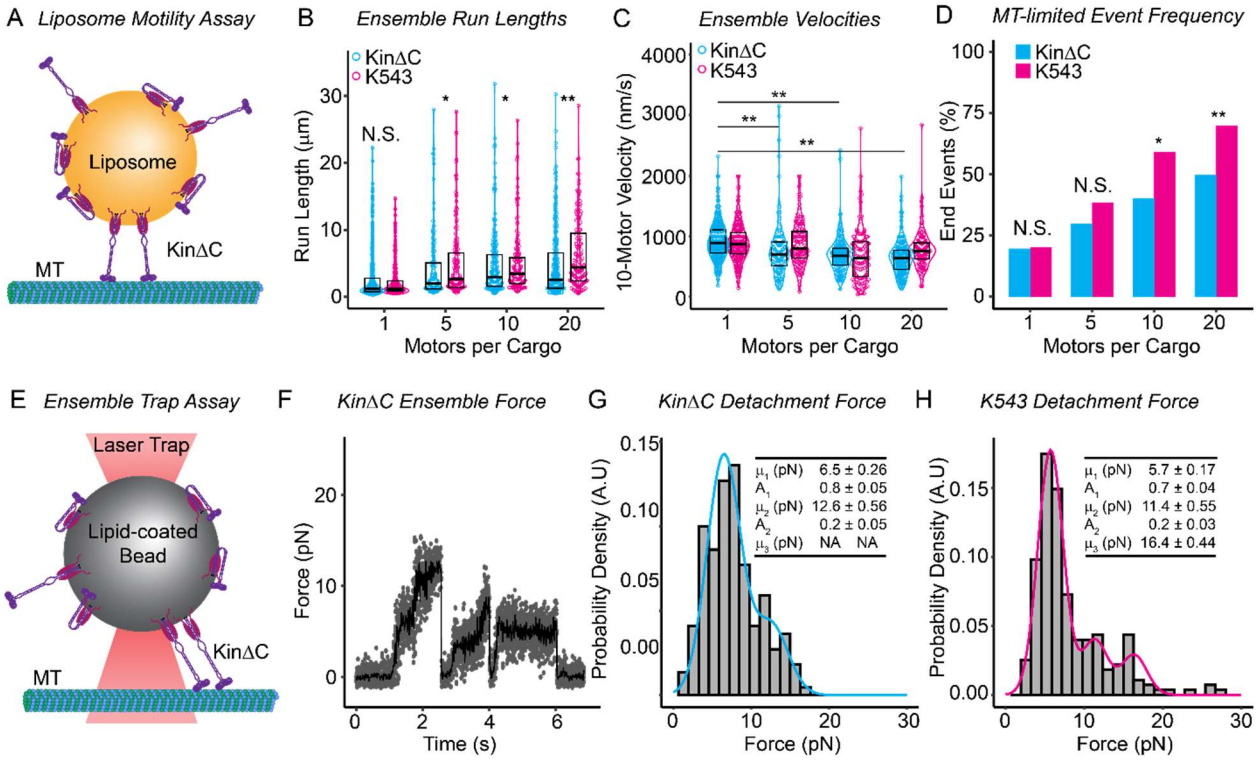


Figure 2 *KinΔC Ensembles Favor Fewer Engaged Kinesins than K543 Ensembles.* (A) Schematic representation of multi-motor motility assay with fluid-like liposome as cargo. Liposome (gold) has 5-20 kinesins (purple) bound to its surface. The fluorescence of the liposome is tracked by TIRF microscopy as it is moved along MTs (green) by the bound kinesins. (B) Dot plots with overlaid violin plots representing multi-motor run lengths measured for KinΔC (cyan) and K543 (magenta) with up to 20 bound kinesins. Black overlaid box plot shows median and upper and lower quartiles per condition. K543 control data are replotted from Bensel et al., 2024. p-Values are as follows: N.S.: p>0.05, *: p<0.05, **: p<0.01. Run length data are compared using a Kruskal-Wallis with Dunn's post-hoc test using the Benjamin-Yuketieli adjustment. See Table S1 for exact p-values. For KinΔC data, $N_{events}$ ranges from 137 – 480 from at least 3 independent experiments. (C) Dot plot with overlaid violin plot representing multi-motor velocities measured for KinΔC (cyan) and K543 (magenta). Black overlaid box plot shows median and upper and lower quartiles per condition. K543 control data are replotted from Bensel et al., 2024 . p-Values are as follows: N.S.: p>0.05, *: p<0.05, **: p<0.01. Velocity data

are compared using a Kruskal-Wallis with Dunn's post-hoc test using the Benjamin-Yuketieli adjustment. See Table S1 for exact p-values. N's are the same as in (B). (D) Bar graph depicting the percentage of runs for each condition (single kinesin Qdot, and 5, 10, and 20 kinesins per liposome) which reach the end of the MT before detaching. K543 data are replotted from Bensel et al., 2024. End event frequencies are compared using a two proportions Z-test. p-Values are as follows: N.S.: $p>0.05$, *: $p<0.05$, **: $p<0.01$. See Table S1 for exact p-values. N's are the same as in (B, C). (E) Schematic representation of multi-motor optical trapping assay with lipid-coated bead as cargo. Kinesins (purple) are bound to lipid-coated beads (grey) in a 20 to 1 excess. The laser trap (red) is used to position the bead close to a MT (green) and force ramps are recorded. (F) Sample force ramp collected for a lipid-coated bead coated with 20 Kin∆C motors. Raw data is shown in grey with median-filtered data overlaid in black. (G) Detachment force histogram with overlaid double Gaussian fit collected for Kin∆C experimental results (cyan). Fit parameters ± fitting error are shown in inset. $N_{events}$ = 169 from 5 independent experiments. (H) Detachment force histogram with overlaid triple Gaussian fit collected for K543 (magenta). K543 data and fit are replotted from Bensel et al., 2024. Fit parameters ± fitting error are shown in inset.

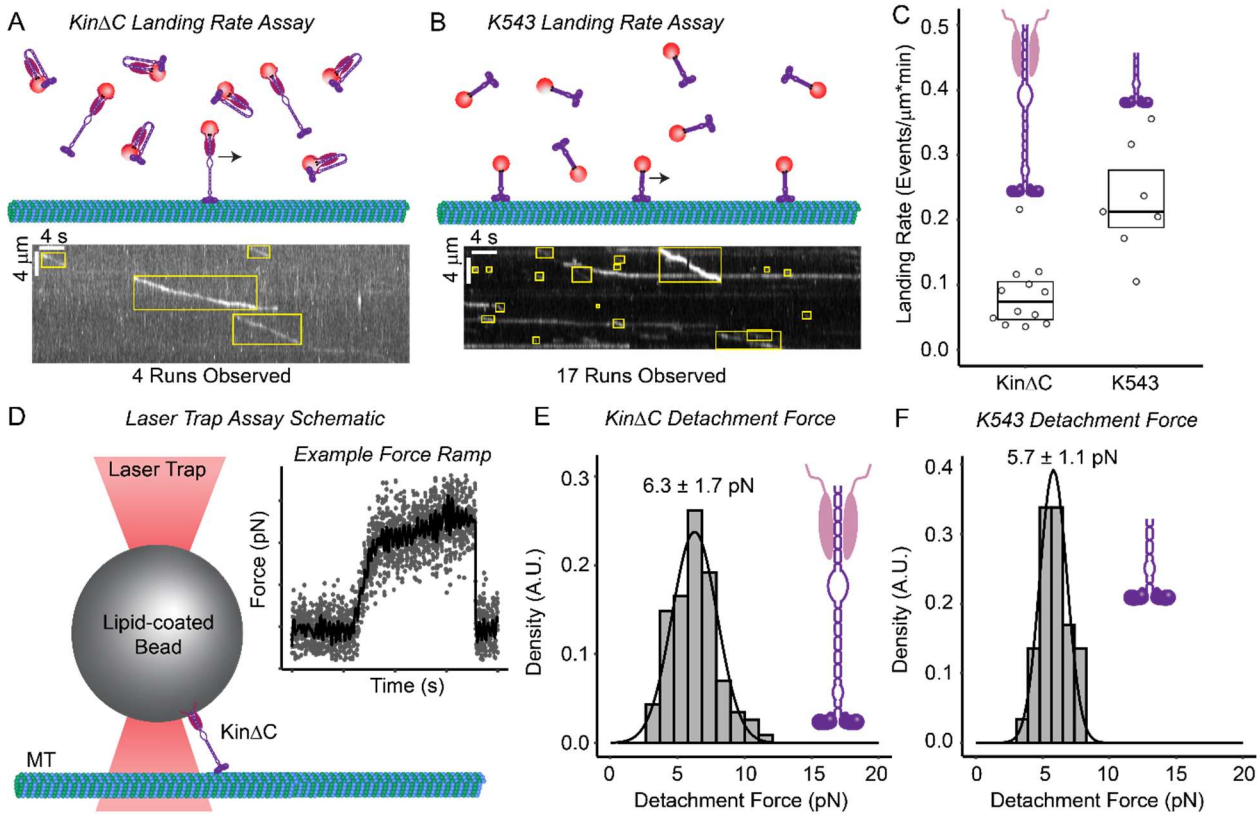


Figure 3. *KinΔC and K543 are indistinguishable once engaged with the MT.* (A, upper) Schematic of landing rate assay as performed with KinΔC. KinΔC is bound to Qdots (red) and flowed into a microscopy chamber containing MTs (green). (A, lower) Example kymograph of single molecule Qdot assay with KinΔC. Runs are boxed in yellow. Distance along MT is represented by the vertical axis while time is represented as the horizontal axis. A moving particle appears as a slanted line while a stuck particle appears as a vertical line. (B, upper) Schematic of landing rate assay as performed with K543. K543 is bound to Qdots (red) and flowed into a microscopy chamber containing MTs (green). (B, lower) Example kymograph of single molecule Qdot assay with K543. Runs are boxed in yellow. Axes are as in (A). (C) Dot plot with overlaid box plot for landing rate determined for KinΔC (left) and K543 (right). Each dot represents the landing rate determined for a single MT in a single video with the equation: Landing Rate = $N_{runs}$/[MT length (µm) x video length (min)]. Statistical analysis was performed using Kruskal-Wallis with Dunn's post-hoc test using Benjamin-Yuketieli adjustment, p = 0.01.

N= 12 MTs (Kin∆C) or 7 MTs (K543) from 3 independent videos each. (D) Schematic representation of single-molecule optical trapping assay as performed. A lipid-coated silica bead (grey) with a bound Kin∆C (purple) is brought close to a surface-bound MT (green) by the laser trap (red). (D, Inset) Sample force ramp collected from a single kinesin-∆C molecule in the optical trapping assay. Median-filtered trace (black) is overlaid on top of raw data (grey). (E) Histogram with overlayed fit of detachment forces measured for single Kin∆C molecules. Kin∆C has a fitted mean detachment force of 6.3 ± 1.7 pN. $N_{events}$ = 109 from 4 independent experiments. (F) Histogram with overlayed fit of detachment forces measured for single K543 molecules. K543 has a fitted mean detachment force of 5.7 ± 1.1 pN. K543 run detachment force data are replotted from Bensel et al., 2024.

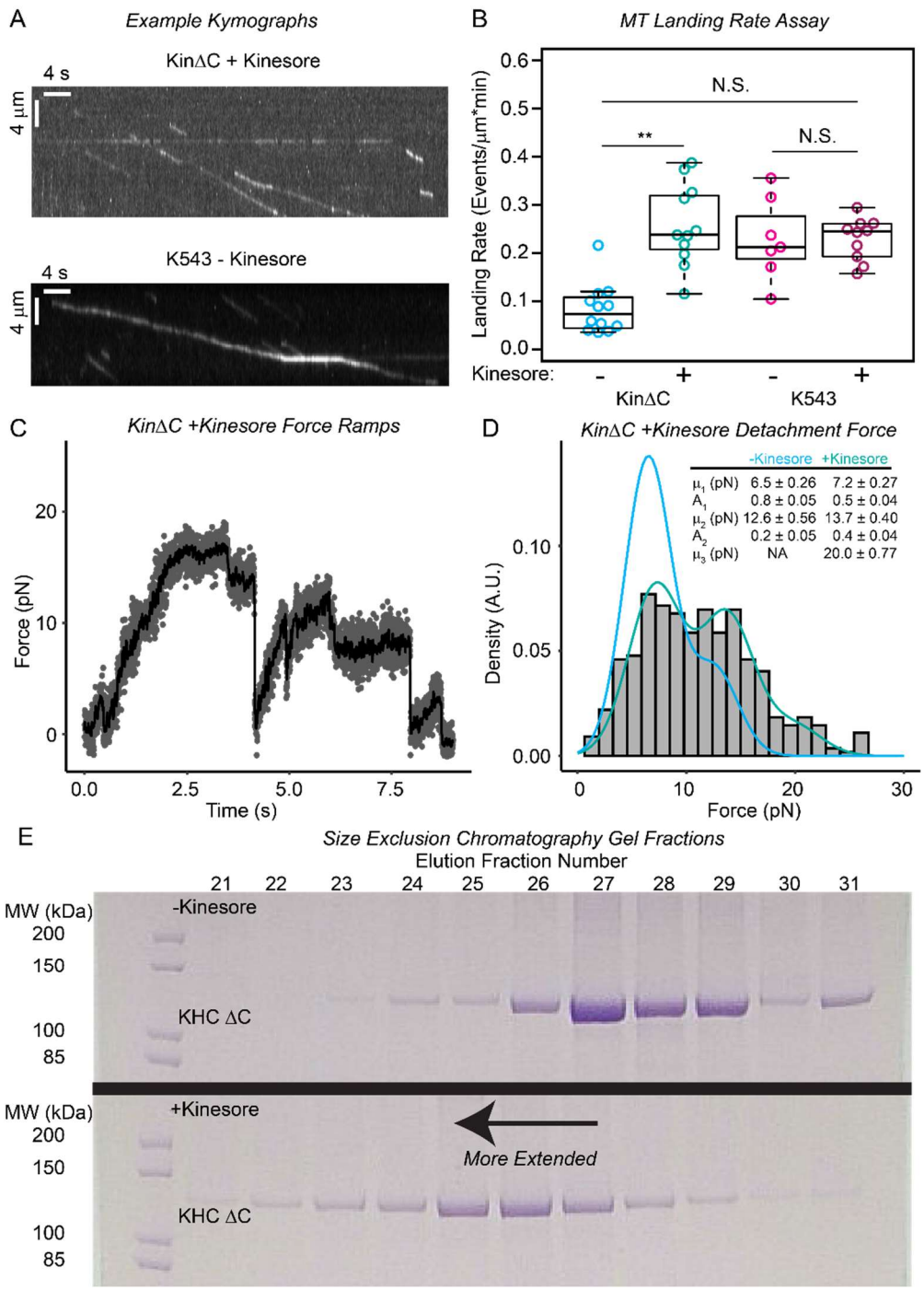


Figure 4. *Kinesore restores the MT engagement activity of KinΔC to that of K543.* (A) Representative landing rate assay kymographs for KinΔC (top) and K543 (bottom) in the presence (top) or absence (bottom) of 50 μM kinesore. Distance is shown on the horizontal axis, while time is shown on the vertical axis. (B) Dot plot of landing rates measured in the absence (-

) and presence (+) of 50 μM kinesore for Kin∆C (cyan, turquoise) and K543 (magenta, burgundy). Each dot represents the landing rate determined from a single MT in a single video. Statistical analysis of landing rate data was performed using Kruskal-Wallis with Dunn's post-hoc test using the Benjamin-Yuketieli adjustment. p-Values are as follows; N.S.: $p>0.05$, **: $p<0.01$. Kin∆C + kinesore, $N_{events}$ = 11 MTs from 3 independent videos, K543 + kinesore, $N_{events}$ = 10 MTs from 3 independent videos. (C) Sample force ramp recorded from a lipid-coated bead being moved by 20 Kin∆C motors in the presence of kinesore. Raw data are shown in grey and median filtered data are overlaid in black. (D) Histogram with overlaid triple Gaussian fit for detachment forces measured Kin∆C in the presence of kinesore (turquoise) with the double Gaussian fit to detachment forces measured for Kin∆C in the absence of kinesore (cyan) shown as reference. $N_{events}$ = 418 from 4 independent experiments. (E) SDS-PAGE of size exclusion chromatography elution fractions for Kin∆C in the absence (top) or presence (bottom) of 50 μM kinesore. Elution fractions are shown increasing from left to right, the band corresponding to the Kin∆C heavy chain (KHC ∆C) is shown. Given the same molecular weight, a molecule will elute sooner the more extended it is.

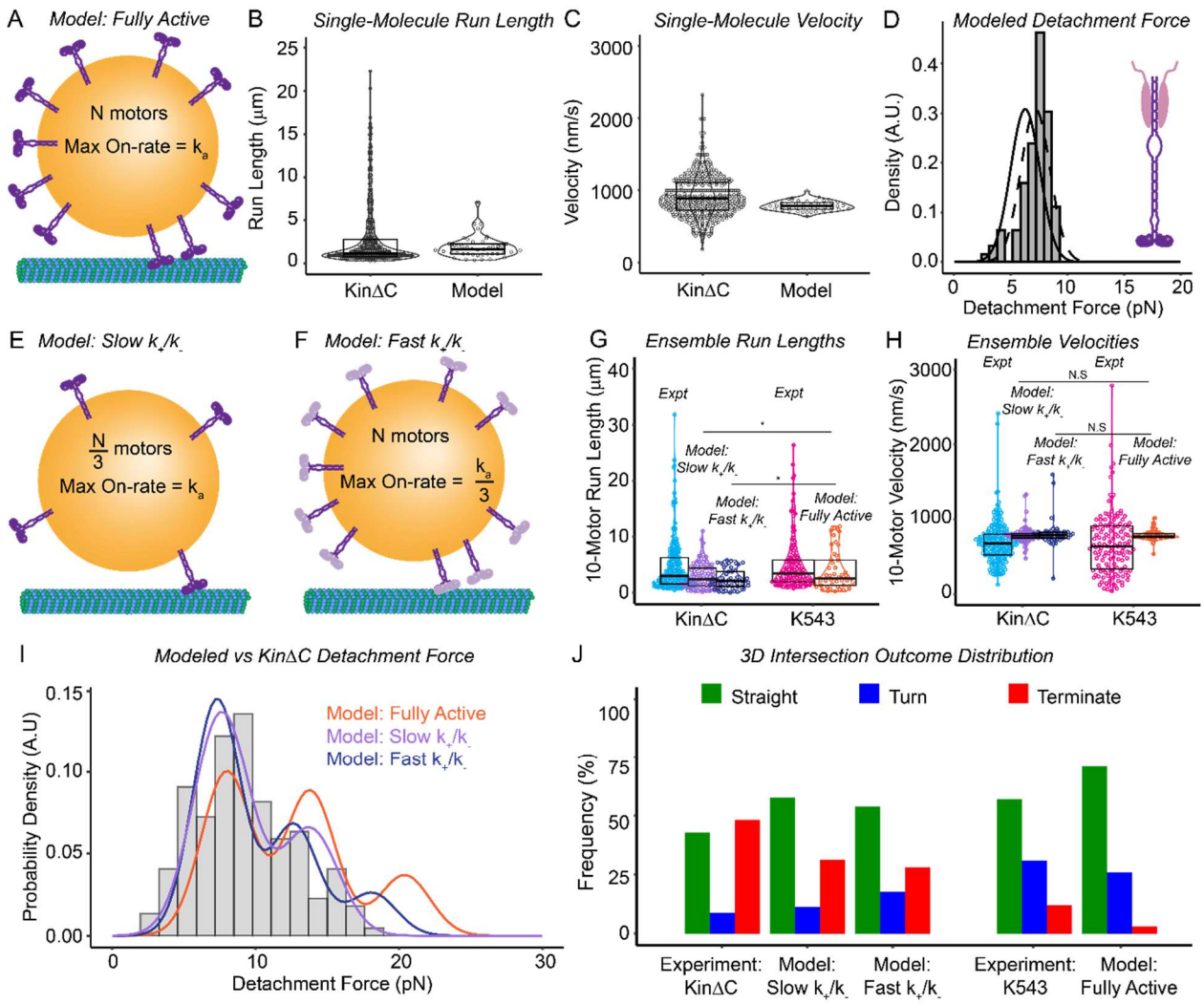


Figure 5. *Mechanistic modeling of kinesin-1 autoinhibition predicts experimental differences observed between KinΔC and K543.* (A) Schematic representation of our mechanistic model of kinesin-1 transport as published in Bensel et al., 2024. All motors in the model are active and bind MTs with a maximum rate $k_a$ = 150 $s^{-1}$. We refer to this as the 'fully active' model. (B) Dot plot with overlaid box plot and violin plot of KinΔC (left) and modeled (right) single molecule run length. Model $N_{events}$ = 46. (C) Dot plot with overlaid box plot and violin plot of KinΔC (left) and modeled (right) single molecule velocity. Model $N_{events}$ = 46. (D) Histogram of modeled detachment force distribution with overlaid single Gaussian fit (black, dashed). Single Gaussian fit to KinΔC detachment force experimental data shown for reference (black, solid). Model $N_{events}$

= 99. (E) Schematic representation of our modified mechanistic model of kinesin-1 which emulates an autoinhibited motor where exchange between the active and inhibited states occurs slowly. We call this model “Slow $k_+/k_-$“ and it is implemented by reducing the number of motors in the simulation by a factor of 3, i.e., N/3 motors. All other model parameters remain the same. (F) Schematic representation of our modified mechanistic model of kinesin-1 which is modified to capture an autoinhibited motor that exchanges rapidly between the active and inhibited states. We call this model “Fast $k_+/k_-$“ and it is implemented by reducing maximum rate of MT association by a factor of 3 to $k_a$ = 50 $s^{-1}$, but no other parameters of the model are changed. (G) Dot plot with overlaid violin plot and box plot of run lengths measured for experimental (Expt) and modeled liposomes with ~10 bound motors. Kin∆C experimental results are shown for reference (cyan) next to the model of Slow $k_+/k_-$ (purple) ($N_{events}$ = 93) and Fast $k_+/k_-$ (dark blue) ($N_{events}$ = 50). K543 experimental results (magenta) and fully active model results (orange) are replotted from Bensel et al., 2024 and shown for reference. Statistical analysis of run length data was performed using Kruskal-Wallis with Dunn’s post-hoc test using the Benjamin-Yuketieli adjustment. p-Values are as follows; N.S.: $p>0.05$, *: $p<0.05$. (H) Dot plot with overlaid violin plot and box plot of velocities measured for experimental (Expt) and modeled liposomes with ~10 bound motors. Kin∆C experimental results are shown for reference (cyan) next to the model of Slow $k_+/k_-$ (purple) and Fast $k_+/k_-$ (dark blue). K543 experimental results (magenta) and fully active model results (orange) are replotted from Bensel et al., 2024 and shown for reference. Statistical analysis of run length data was performed using Kruskal-Wallis with Dunn’s post-hoc test using the Benjamin-Yuketieli adjustment. p-Values are as follows; N.S.: $p>0.05$. (I) Histogram of experimentally measured detachment forces for ensembles of 20 Kin∆C with overlaid model prediction fits. The model of Slow $k_+/k_-$ is shown in purple ($N_{events}$ = 200), Fast $k_+/k_-$ is shown in dark blue ($N_{events}$ = 200), and fully active model is shown in orange. Fully active model fit is replotted from Bensel et al., 2024. (J) Bar graph of 3D intersection

outcomes for experiments and simulations. Slow $k_+/k_-$ $N_{events}$ = 285, fast $k_+/k_-$ $N_{events}$ = 260. K543 experimental results and fully active model results are replotted from Bensel et al., 2024.